



LUND UNIVERSITY

Present and future precipitation variations in the source region of the Yangtze River, China

Du, Yiheng

2021

Document Version:

Publisher's PDF, also known as Version of record

[Link to publication](#)

Citation for published version (APA):

Du, Y. (2021). *Present and future precipitation variations in the source region of the Yangtze River, China*. [Doctoral Thesis (compilation), Lund University]. Water Resources Engineering, Lund University.

Total number of authors:

1

General rights

Unless other specific re-use rights are stated the following general rights apply:

Copyright and moral rights for the publications made accessible in the public portal are retained by the authors and/or other copyright owners and it is a condition of accessing publications that users recognise and abide by the legal requirements associated with these rights.

- Users may download and print one copy of any publication from the public portal for the purpose of private study or research.
- You may not further distribute the material or use it for any profit-making activity or commercial gain
- You may freely distribute the URL identifying the publication in the public portal

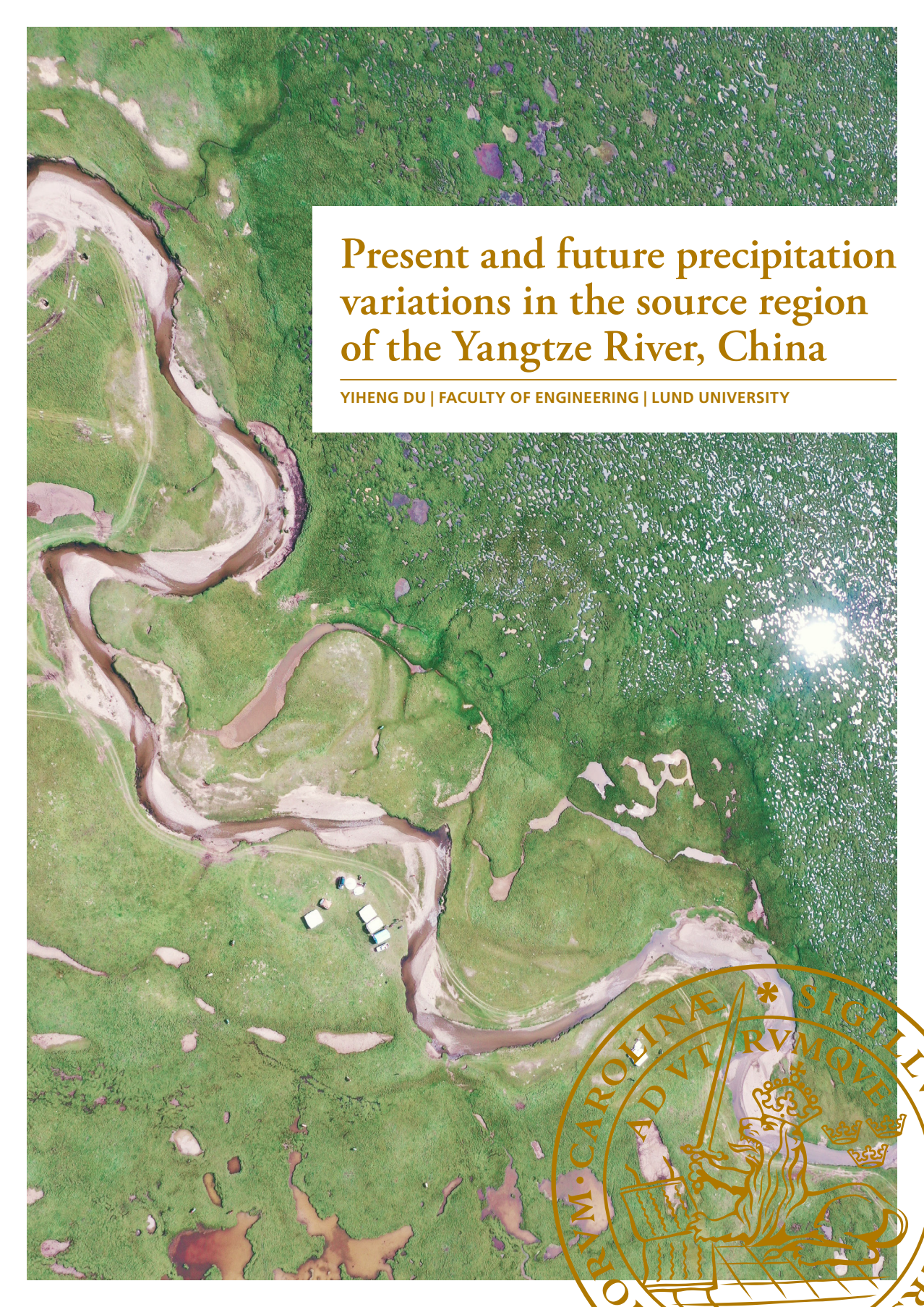
Read more about Creative commons licenses: <https://creativecommons.org/licenses/>

Take down policy

If you believe that this document breaches copyright please contact us providing details, and we will remove access to the work immediately and investigate your claim.

LUND UNIVERSITY

PO Box 117
221 00 Lund
+46 46-222 00 00

An aerial photograph of a river meandering through a lush green landscape. The river is a light brown color, contrasting with the vibrant green of the surrounding vegetation. The river flows from the top left towards the bottom right, forming several loops and curves. In the bottom right corner, there is a circular seal with a golden border. Inside the seal, there is a figure holding a sword and a shield, with the text 'SIGILLUM' at the top, 'PVM CAROLINAE' on the left, and 'ADVT RVMQVE' on the right. The background of the entire slide is the aerial photograph.

Present and future precipitation variations in the source region of the Yangtze River, China

YIHENG DU | FACULTY OF ENGINEERING | LUND UNIVERSITY



There is an old Chinese saying: when you are taking water from a river, be grateful for the source. As I grow up in a city downstream the Yangtze River, everything I live on comes from the river, clean water, various food, and beautiful scene. This thesis is my sincere gratitude for the source of the river. Without carefully protection of the source region, there will be no prosperous in the downstream. Climate change is a mutual challenge for all human beings, and I'd like to contribute my efforts and stand together with our mother nature.

Present and future precipitation variations in the source region of the Yangtze River, China

Present and future precipitation variations in the source region of the Yangtze River, China

Yiheng Du



LUND
UNIVERSITY

DOCTORAL DISSERTATION

by due permission of the Faculty of Engineering, Lund University, Sweden.
To be defended at the Faculty of Engineering, V-building, John Ericssons väg 1,
Lund, room V:C on 2nd March, 2021 at 10:15 a.m.

Faculty opponent
Prof. Dr. Deliang Chen
University of Gothenburg

Organization LUND UNIVERSITY Division of Water Resources Engineering P.O. Box 118 SE-221 00 Lund Sweden		Document name Doctoral Thesis, report TVVR-1087 (2021)	
Author Yiheng Du		Date of issue Mar 2nd, 2021	
		Sponsoring organization Chinese Scholarship Council (CSC)	
Title and subtitle Present and future precipitation variations in the source region of the Yangtze River, China			
Abstract <p>The source region of the Yangtze River (SRYR), the origin of the longest river in China, is an area with high-mountains and river ecotones that face considerable challenges under climate change. Precipitation is fundamental for sustainable ecosystems in this area and for the downstream water supplies. Thus, this study investigated the present and future patterns of precipitation variation in the SRYR.</p> <p>To investigate historical climate characteristics of the SRYR, analysis of hydro-climatic components during 1957-2013 was performed. Temperature in the SRYR increased at a rate of 0.34°C/decade, precipitation and evaporation increased by 11.4 and 7.6 mm/decade, respectively. Runoff depth increased by 3.3 mm/decade. Considering the water balance, annual water storage was constant despite a continuous small negative trend. Increase in precipitation is mainly caused by increasing evapotranspiration, leading to the relatively stable water storage during the study period, which also suggests an accelerating water cycle in the SRYR. This knowledge is essential for the understanding of water resources conditions in the area.</p> <p>Rainy season precipitation (June-August) in the SRYR accounts for approximately 70% of the annual total, and its anomalies are essential for ecosystem resilience. Hence, analysis of rainy season precipitation variability in relation to sea surface temperature (SST) anomalies as well as large-scale circulations including El Niño Southern Oscillation (ENSO) and Pacific Decadal Oscillation (PDO) was conducted. Results indicate that the leading modes of rainy season precipitation variability can be explained by the variability of SST together with an integrated effect of ENSO and PDO. The influence of ENSO and PDO will enhance/decrease when they are in-/out-of-phase, respectively. Negative PDO induces more precipitation in La Niña years than in El Niño years for the SRYR, especially over central and eastern parts of the basin. Positive PDO induces precipitation decrease, and El Niño enhances the decrease. The mechanism behind this pattern is atmospheric circulation affecting the strength of westerlies that transport moisture to the inland areas and as well local convergence conditions. Results have implications for predicting the rainy season precipitation for coming decades over the study area. If the current negative PDO phase continues together with more frequent extreme La Niña events, as suggested in other research, more precipitation during rainy season is expected over the SRYR.</p> <p>To further quantify precipitation variability, a multi-space model for seasonal precipitation prediction was developed using principal component analysis (PCA) and artificial neural network (ANN). Correlation analysis shows that the most important climate indices for precipitation in the SRYR vary depending on the season and spatial location. The North Atlantic Oscillation (NAO), Polar/Eurasia Pattern (POL), Southern Oscillation Index (SOI), and Scandinavia Pattern (SCA) events have influence on precipitation in the SRYR during the cold season, while NAO, PDO, and SOI are more important for the warm season. A spatiotemporal model for predicting grid precipitation using significant correlated indices was established for each season, the PCA-ANN model. Results show that the PCA-ANN model can predict precipitation in the study area. By reconstructing principal components, the model provides a simulated dataset with the same size as the original dataset. The PCA-ANN model performs well in terms of both temporal variability and spatial distribution following the rank summer> winter> spring> autumn. A small basin with many variables/grids is recommended for the PCA-ANN model.</p> <p>To access future precipitation pattern, historical performance, and future projections of monthly precipitation in the SRYR were investigated, using the National Aeronautics Space Administration (NASA) Earth Exchange Global Daily Downscaled Projections (NEX-GDDP) dataset. Performance of the 21 models were compared against in situ observations for the historical period 1961–2005, therefore rankings were listed according to their performance. Projected future changes in precipitation were assessed under the Representative Concentration Pathways (RCPs) 4.5 and 8.5 emission scenarios, for near-future (2041-2060) and far-future (2081–2100) time slices with respect to 1986–2005. The results show that models derived from NEX-GDDP data effectively produce observed precipitation magnitude in the study area and optimum models were selected based on comprehensive ranking index. The future climate projections indicate a consistent rise in mean precipitation, especially in summer. The average annual precipitation during the near-future and the far-future showed an increase of 18.6% and 24.4% under RCP 4.5, and a larger increase under RCP 8.5 of 22.5% and 49.7%. The summer precipitation shows similar increase as the annual precipitation but with a slightly larger amplitude.</p> <p>The findings in this thesis provide insights to improve the understanding of water resources variations under the background of climate change, and to establish sustainable management of water resources. The precipitation variability in relation to large-scale circulation can help to improve weather forecasting at a low-cost level. Besides, identification of physical mechanisms of integrated impacts from two major circulation patterns can improve the understanding of drivers behind precipitation variability. Future projections provide guidance for future adaptive solutions, including both spatial and temporal changes. With such information, adaptive plans for the study area can be set up with higher accuracy, lower budget, and localized suitability.</p>			
Key words: Precipitation; climate change; climate variability; teleconnection; water balance; ENSO; PDO; future projections; the source region of Yangtze River; Tibet Plateau.			
Classification system and/or index terms (if any)			
Supplementary bibliographical information		Language: English	
ISSN and key title 1101-9824		ISBN 978-91-7895-739-2 (print) 978-91-7895-740-8 (pdf)	
Recipient's notes		Number of pages 147	
		Price	
		Security classification	

I, the undersigned, being the copyright owner of the abstract of the above-mentioned dissertation, hereby grant to all reference sources permission to publish and disseminate the abstract of the above-mentioned dissertation.

Signature 杜一衡

Date 2021-Jan-14th

Present and future precipitation variations in the source region of the Yangtze River, China

Yiheng Du



LUND
UNIVERSITY

Cover photo by Yong Zhang(张永)

Copyright 2021 Yiheng Du

Faculty of Engineering, Department of Building and Environmental Technology,
Division of Water Resources Engineering

Paper 1 © by MDPI

Paper 2 © by John Wiley and Sons

Paper 3 © by MDPI

Paper 4 © by the authors (Manuscript)

ISBN 978-91-7895-739-2 (print)

ISBN 978-91-7895-740-8 (pdf)

ISSN 1101-9824

Report No.TVVR-1087

Printed in Sweden by Media-Tryck, Lund University
Lund 2021



Media-Tryck is a Nordic Swan Ecolabel
certified provider of printed material.
Read more about our environmental
work at www.mediatryck.lu.se

MADE IN SWEDEN 

健康，平安，爱

Table of Contents

Popular summary	i
Populärvetenskaplig sammanfattning	iii
Abstract	v
摘要	vii
Acknowledgements	ix
Papers	xi
Abbreviations and symbols	xiii
List of figures	xv
List of tables	xv
1. Introduction	1
2. Theoretical background	3
2.1. Climate variability and climate change	3
2.2. Large-scale circulation patterns	4
2.3. General circulation models and NEX-GDDP dataset	7
3. Study area	9
4. Data	11
4.1. Climate variables	11
4.2. Large-scale circulation	12
4.3. Reanalysis data	12
4.4. NEX-GDDP dataset	13
5. Methods	15
5.1. Statistical analysis	15
5.2. Water balance and uncertainty	16
5.3. Water moisture convergence	18
5.4. Simulation model using large-scale circulation patterns	19
5.5. Future precipitation pattern using NEX-GDDP dataset	21

6. Results and discussion	23
6.1. Historical climate change	23
6.1.1. Trend analysis on basin scale	23
6.1.2. Water balance and uncertainty analysis.....	23
6.1.3. Spatial pattern.....	24
6.2. Precipitation variability using teleconnections.....	27
6.2.1. Correlation with large-scale circulation pattern	27
6.2.2. Integrated impact of large-scale circulation for rainy season	29
6.2.3. Simulation of precipitation using large-scale circulation	33
6.3. Future precipitation pattern	36
6.3.1. Performance evaluation	36
6.3.2. Projections of the future	39
7. Conclusions and outlook	43
7.1. Conclusions.....	43
7.2. Suggestions	45
7.3. Future studies	46
References	47

Popular summary

Across the Himalaya mountains, in the inner land of the Tibet Plateau, you find the source region of the Yangtze River, the origin of the third-longest river in the world. It is a cold, barren, isolated area in the mountains where it is difficult for plant, animal, human or even observational equipment to survive. Climate change is raising more and more problems in this area, such as unstable conditions of grassland, decreasing number of plants, melting of glaciers, and so on. The local government struggles to balance economic development and environmental protection. To be able to take the right actions, they first need to know key factors for climate change: rainfall. This is where our study can help.

How will rainfall change from the past to the future? First, we detected a trend of climate variables for the past 50 years and found that rainfall amount in this area increased significantly. Water storage was constant despite a continuous small negative trend. To investigate the future, climatologists provide us simulation results under different greenhouse gas emission scenarios. After comparing and analysing the future rainfall in this area, huge increase was revealed by our analysis. If we take intermediate control of the greenhouse gas emission, the rainfall may increase by 25% by the end of 21st century. If we take no control of the greenhouse gas emission, the increase will double. A far-reaching plan is needed on the top list of the local governments.

Beside the long-term change, the rainfall varies year to year. As rainfall comes from water vapor in the atmosphere, wind and temperature of land or ocean surface can influence the rainfall by changing the water vapor circulation, sometimes even at a considerable distance, which we call teleconnection. We found that two teleconnection patterns show a close relation with summer rainfall in our study area: El Niño–Southern Oscillation (ENSO) and Pacific Decadal Oscillation (PDO). These patterns are indices for the surface thermal condition of the Pacific Ocean. We found that more rainfall occurs in our study area during cold PDO years, particularly when cold PDO and cold ENSO coincide. This means 6% more rainfall than usual. In contrast, warm PDO brings dryness to the area, and warm ENSO makes it even drier, with up to 10% less than average rainfall. When cold PDO occurs with warm ENSO or the opposite happens, warm PDO with cold ENSO, their influence compensates, and the change in rainfall is marginal. The reason behind is, the combination of ENSO and PDO affects the strength of the wind that transports moisture to our study area and the intensity of ascending movement. Such information is extremely useful since it offers us a way of predicting a changing future. According to many studies, a cold PDO phase may continue until 2050. Also, extreme El Niño (warm ENSO) and La Niña (cold ENSO) events both tend to increase due to greenhouse gas emissions. This means that we can expect more extreme ENSO years combined with a cold PDO phase in the future. In this scenario,

more rainfall is likely to fall in the study area, especially during extreme La Niña years.

Our findings provide insights to improve the understanding of rainfall change. The considerable increase of future rainfall provides local government with guidance for adaptive solutions. The rainfall variation in relation to teleconnections can help to improve rainfall forecasting at a low-cost level. With such information, the local authorities can prepare the study area for rainfall change with higher accuracy, lower budget, and localized suitability.

Populärvetenskaplig sammanfattning

Tvårs över Himalayabergen, i det inre av Tibet-platån, hittar man källregionen till Yangtze-floden, ursprunget till den tredje längsta floden i världen. Det är ett kallt, kargt, isolerat område i bergen där det är svårt för växter, djur, människor och till och med observationsutrustning att överleva. Klimatförändringar innebär fler och fler problem i detta område, såsom instabilt tillstånd för gräsmark, minskat antal växter, smältning av glaciärer och så vidare. De kinesiska myndigheterna kämpar för att balansera ekonomisk utveckling med miljöskydd. För att kunna vidta rätt åtgärder måste man först veta hur klimatförändring kommer att påverka nederbörden. Det är här vår studie kan hjälpa.

Hur kommer regnet att förändras i framtiden? Först upptäckte vi en trend för klimatvariabler under de senaste 50 åren och fann att regnmängden i detta område ökade betydligt. Vattenupplagringen var konstant trots en kontinuerlig liten negativ trend. För att undersöka framtida förändringar ger klimatologer oss simuleringsresultat under olika växthusgasutsläppsscenarier. Dessa redskap indikerar att nederbörden kommer att öka i framtiden. Om växthusgasutsläppen minskar, kan nederbörden att öka med 25% till ca 2100. Om vi inte minskar växtgasutsläppen kan nederbörden fördubblas. En långtgående plan behövs för att anpassa området till dessa förändringar.

Förutom den långsiktiga förändringen varierar nederbörden också från år till år. Eftersom regn kommer från vattenånga i atmosfären kan vind och temperatur påverka regnmängden genom ändrad vattenångcirkulationen, ibland till och med på ett betydande avstånd, som vi kallar telekoppling. Vi fann att två telekopplingsmönster visar ett nära samband med somrarnederbörden i vårt studieområde: El Niño – Southern Oscillation (ENSO) och Pacific Decadal Oscillation (PDO). Dessa mönster är index för Stilla Havets termiska tillstånd. Vi fann att mer nederbörd faller i vårt studieområde under de kalla PDO-åren, särskilt under åren med kall PDO och kall ENSO, då det faller 6% mer nederbörd än vanligt. Däremot ger varm PDO torrt klimat, och varm ENSO gör det ännu torrare, med upp till 10% mindre nederbörd. När kall PDO uppträder med varm ENSO eller motsatsen händer, varm PDO med kall ENSO, kompenserar de varandra och nederbördsförändringen blir marginell. Anledningen till detta är att kombinationen av ENSO och PDO påverkar vindstyrkan som transporterar fukt till vårt studieområde och intensiteten i stigande luftmassor. Sådan information kan vara extremt användbar eftersom den ger oss ett sätt att förutsäga framtida nederbördsförändringar. Enligt många studier kan en kall PDO-fas fortsätta fram till 2050. Extrema El Niño (varm ENSO) och La Niña (kall ENSO) händelser tenderar också att öka på grund av växthusgasutsläpp. Detta innebär att vi kan förvänta oss mer extrema ENSO-år i kombination med en kall PDO-fas i framtiden. I detta scenario kommer sannolikt mer nederbörd att falla i studieområdet, särskilt under extrema La Niña-år.

Våra resultat ger insikter som gör att förståelsen för nederbördsförändringar förbättras. Den betydande ökningen av framtida nederbörd ger de kinesiska myndigheterna vägledning för att anpassa området för framtiden. Regnvariationen i förhållande till växtgasutsläpp kan hjälpa till att förbättra prognoser för framtiden till en låg kostnad. Med sådan information kan de lokala myndigheterna förbereda studieområdet för regnförändringar med högre noggrannhet, lägre budget och lokal lämplighet.

Abstract

The source region of the Yangtze River (SRYR), the origin of the longest river in China, is an area with high-mountains and river ecotones that face considerable challenges under climate change. Precipitation is fundamental for sustainable ecosystems in this area and for the downstream water supplies. Thus, this study investigated the present and future patterns of precipitation variation in the SRYR.

To investigate historical climate characteristics of the SRYR, analysis of hydro-climatic components during 1957-2013 was performed. Temperature in the SRYR increased at a rate of $0.34^{\circ}\text{C}/\text{decade}$, precipitation and evaporation increased by 11.4 and 7.6 mm/decade, respectively. Runoff depth increased by 3.3 mm/decade. Considering the water balance, annual water storage was constant despite a continuous small negative trend. Increase in precipitation is mainly caused by increasing evapotranspiration, leading to the relatively stable water storage during the study period, which also suggests an accelerating water cycle in the SRYR. This knowledge is essential for the understanding of water resources conditions in the area.

Rainy season precipitation (June-August) in the SRYR accounts for approximately 70% of the annual total, and its anomalies are essential for ecosystem resilience. Hence, analysis of rainy season precipitation variability in relation to sea surface temperature (SST) anomalies as well as large-scale circulations including El Niño Southern Oscillation (ENSO) and Pacific Decadal Oscillation (PDO) was conducted. Results indicate that the leading modes of rainy season precipitation variability can be explained by the variability of SST together with an integrated effect of ENSO and PDO. The influence of ENSO and PDO will enhance/decrease when they are in-/out-of-phase, respectively. Negative PDO induces more precipitation in La Niña years than in El Niño years for the SRYR, especially over central and eastern parts of the basin. Positive PDO induces precipitation decrease, and El Niño enhances the decrease. The mechanism behind this pattern is atmospheric circulation affecting the strength of westerlies that transport moisture to the inland areas and as well local convergence conditions. Results have implications for predicting the rainy season precipitation for coming decades over the study area. If the current negative PDO phase continues together with more frequent extreme La Niña events, as suggested in other research, more precipitation during rainy season is expected over the SRYR.

To further quantify precipitation variability, a multi-space model for seasonal precipitation prediction was developed using principal component analysis (PCA) and artificial neural network (ANN). Correlation analysis shows that the most important climate indices for precipitation in the SRYR vary depending on the season and spatial location. The North Atlantic Oscillation (NAO), Polar/Eurasia Pattern (POL), Southern Oscillation Index (SOI), and Scandinavia Pattern (SCA)

events have influence on precipitation in the SRYR during the cold season, while NAO, PDO, and SOI are more important for the warm season. A spatiotemporal model for predicting grid precipitation using significant correlated indices was established for each season, the PCA-ANN model. Results show that the PCA-ANN model can predict precipitation in the study area. By reconstructing principal components, the model provides a simulated dataset with the same size as the original dataset. The PCA-ANN model performs well in terms of both temporal variability and spatial distribution following the rank summer> winter> spring> autumn. A small basin with many variables/grids is recommended for the PCA-ANN model.

To access future precipitation pattern, historical performance, and future projections of monthly precipitation in the SRYR were investigated, using the National Aeronautics Space Administration (NASA) Earth Exchange Global Daily Downscaled Projections (NEX-GDDP) dataset. Performance of the 21 models were compared against in situ observations for the historical period 1961–2005, therefore rankings were listed according to their performance. Projected future changes in precipitation were assessed under the Representative Concentration Pathways (RCPs) 4.5 and 8.5 emission scenarios, for near-future (2041–2060) and far-future (2081–2100) time slices with respect to 1986–2005. The results show that models derived from NEX-GDDP data effectively produce observed precipitation magnitude in the study area and optimum models were selected based on comprehensive ranking index. The future climate projections indicate a consistent rise in mean precipitation, especially in summer. The average annual precipitation during the near-future and the far-future showed an increase of 18.6% and 24.4% under RCP 4.5, and a larger increase under RCP 8.5 of 22.5% and 49.7%. The summer precipitation shows similar increase as the annual precipitation but with a slightly larger amplitude.

The findings in this thesis provide insights to improve the understanding of water resources variations under the background of climate change, and to establish sustainable management of water resources. The precipitation variability in relation to large-scale circulation can help to improve weather forecasting at a low-cost level. Besides, identification of physical mechanisms of integrated impacts from two major circulation patterns can improve the understanding of drivers behind precipitation variability. Future projections provide guidance for future adaptive solutions, including both spatial and temporal changes. With such information, adaptive plans for the study area can be set up with higher accuracy, lower budget, and localized suitability.

摘要

长江源区是中国最长河流——长江的发源地，属于中国的高寒生态脆弱区。气候变化引起的源区生态恶化，不仅严重制约了当地的社会、经济和文化发展，对下游地区的用水安全也产生负面影响。因此，本论文系统分析了气候变化背景下长江源区降水的变化趋势及异常特征，以期对该地区的生态保护和建设提供科学依据。

首先，为了掌握长江源区的历史气候特征，本文对 1957 到 2013 年间长江源区的水文气象变量进行了趋势分析。结果表明，在过去五十多年间，长江源区的年平均气温有显著的增长趋势，速率为每十年 0.34°C 。源区的年降水量、年蒸发量、年径流深度则分别以每十年 11.4、7.6、3.3 毫米的速度增加。基于水量平衡原理，本文对流域水储量的变化进行了探究，结果表明源区的水储量基本保持稳定，尽管出现了持续减小的趋势。综合分析得出，源区气温升高引起蒸散量的增加，与降水量的增加相抵，共同维持了水储量的相对稳定；与此同时，也揭示了源区日益加剧的水循环过程。这些信息对于我们进一步掌握该地区的水资源状况至关重要。

在此基础上，本文分析了长江源区雨季降水异常特征及其影响因子。由于长江源区的雨季降水量（6 月至 8 月）约占全年降水量的 70% 以上，掌握其异常特征对于维护生态系统的稳定十分重要。因此，本文深入分析了雨季降水距平值与海平面温度之间的关系，并分析了与厄尔尼诺南方涛动（ENSO）和太平洋年代际涛动（PDO）等大尺度环流模式之间的遥相关关系。结果表明，源区雨季降水距平值与海平面温度的变化以及 ENSO 和 PDO 的相位特征都有着显著关系。值得特别指出的是，ENSO 和 PDO 会对源区降水产生叠加影响。当 ENSO 和 PDO 处于异相位（同相位）时，其综合影响将会削弱（加强）。对于长江源区而言，当 PDO 处于负相位时，雨季降水量整体偏多；拉尼娜年份中当年降水量将进一步增加，而厄尔尼诺年份中这种增加会被削弱，该现象在源区中部和东部表现尤为明显。当 PDO 处于正相位时，源区的雨季降水量整体偏少，厄尔尼诺年份中降水量进一步减少。其原因是大尺度环流模式所代表的不同大气环流强度和水汽通量，影响了向内陆地区输送水汽的西风强度以及源区当地的水汽收敛条件。这项结果对预测源区未来的雨季降水具有重要意义。有研究表明，当前 PDO 负相位状态将持续一段时间，并可能伴有更频繁的极端拉尼娜事件，结合本文的结果，则可以推测长江源区的雨季降水可能出现异常偏多的情况。

为了进一步量化不同季节的降水距平值，本文使用主成分分析（PCA）和人工神经网络（ANN）建立了季节降水的预测模型。首先通过主成分分析将各季节的网格降水数据转化为数个主成分，通过相关分析，得到与各个主

成分相关的气候因子及其滞后相关性，选取显著相关的因子作为自变量输入模型，通过训练人工神经网络建立预测模型，最后通过主成分的逆向重构，生成与原始数据集具有相同维度的预测数据集。相关分析的结果显示，在冬春季节，降水的主要影响因子有北大西洋涛动（NAO）、极地/欧亚大陆模式（POL）、南方涛动指数（SOI）和斯堪的纳维亚模式（SCA），而在夏秋季节，则是 NAO、PDO 和 SOI 的影响更为显著。模型评估结果表明，本文所提出的 PCA-ANN 模型对于预测研究区域的降水表现良好，对于时间尺度和空间分布的特征都有较好反应，其综合表现优劣顺序为：夏季，冬季，春季，秋季。此结果对于了解源区降水距平值提供了可靠的量化依据。

为了进一步研究未来情景下长江源区的降水模式，本文采用美国国家航空航天局发布的 NEX-GDDP 高分辨率统计降尺度模型数据集，对该数据集内的 21 个模式在长江源区的历史表现和未来降水进行了研究。将 1961-2005 年间的模型降水与实测降水进行了深入比较，结果表明该数据集对长江源区的月降水表现出了较强的模拟能力。根据泰勒图和综合指数排序结果，本文对模式进行了进一步的优选。基于模型优选和多模式平均的结果，本研究对于两种典型排放情景 RCP4.5 和 RCP8.5 下，近未来（2041-2060）和远未来（2081-2100）期间的年降水量，相对于基准期（1986-2005）的变化幅度进行了评估。结果表明，未来的降水量将持续增加，尤其是夏季降水。近未来和远未来的年平均降水量在 RCP4.5 下分别增加了 18.6% 和 24.4%，在 RCP8.5 下则增加了 22.5% 和 49.7%。夏季降水量与年降水量增长整体一致，但幅度更大。

本论文的研究结果有利于提高气候变化背景下，对长江源区水资源变化的认识，为建立可持续的水资源管理体系提供科学指导。与大尺度环流相关的降水变异性分析有助于在较低成本水平上实现降水预报。此外，从两个主要环流模式中识别其叠加作用的机制，有助于提高对降水变异性机理的认识。对未来降水变化的分析结果则为今后适应性的解决方案指明了工作方向。这些信息对于在长江源区制定更准确、更经济、更因地制宜的水资源规划将起到不可或缺的作用。

Acknowledgements

Finally! The most important chapter!

I've dreamed of writing acknowledgments many times. But right now, at this moment, I still feel my words are too limited. During the past years of PhD work, there're thousands of moments that I feel I am so lucky to be here.

First of first, I'd like to express my deepest gratitude to my main supervisor, **Professor Ronny Berndtsson**. As a lighthouse of my PhD journey, you always guide me in the right direction with your professional vision. Every time I came to you with a big problem which already bothered me for some time, you tackled it as you have a magic wand. Your high efficiency of work always surprises and cherishes me. The valuable qualities in your personality is a lifelong guidance for me.

Thanks to **Professor Cintia B. Uvo** for your kindly supervision. The help you gave me is priceless. You lead me into the fantastic world of statistical analysis, which is fundamental to my PhD work.

Thanks to my co-supervisor Professor **Linus Zhang**, for always being encouraging and warm-hearted. And thanks for all the nice meals you prepare which fill in the empty heart of being far away from China.

Thanks to my friend and co-supervisor, **Dr. Feifei Yuan**, for being so helpful with all the grants application, thesis writing, and psychological counseling. Thank you for your generous help by sharing your knowledge and experience.

Big appreciation is given to my co-authors, for informative discussions and critical insights. Special thanks to **Professor Zhenchun Hao** and **Professor Qin Ju** from Hohai University, for your support in method improvements and data access.

Now I want to express my sincere gratitude to all the people I met during my PhD life. Because of you, PhD is not only a journey of academic research, but also a journey to see the wonderful world.

Big hugs to **Shifteh Mobini**, for being a colleague, a friend, and a family. The time spent with you wiped out all my loneliness of being abroad and gave me the feeling of being home in Sweden. And because of you and dearest **Emil** of course, now I'm a big fan of everything related to Iran, food, tea, music, spices and pattern.

Thanks to **Dr. Jing Li** for being a cheerful office roommate. Your personality is like sunshine around; no matter windy, raining or snowing outside (anything like a typical Swedish winter), I always feel warm.

Thanks to **Dr. Claudia Canedo Rosso**. Thank you for all the inspiring academic or non-academic chatting. I always remember the day you explained Principal Component Analysis to me, which cleared all my confusions.

Thanks to dearest **Carina Litttrén**. Thank you for the first hug I ever received in Sweden, and thank you for helping me with all the troublesome tables, bookings and registrations.

Thanks to **everyone in TVRL** for the pleasant and equal atmosphere. Thanks to **all the professors** for the inspiring courses and coffee talks. Special thanks to **Magnus Persson** and **Lars Bengtsson**, for patiently answering my questions and broadening my view in soil and snow research. Thanks to **Catherine** for lively explanation of bacteria and for the nice fika in your rose garden. Thanks to **Peder** for your patience in bearing my broken Swedish. Thanks to **all my colleagues** for sharing and accepting my happiness, depression and self-doubt. Special thanks to **Jie** for delicious hot pots and all the great trips we go together. Thanks to **Johanna**, for showing me various new knowledge in urban hydrology and in baby parenting. Thanks to **Carla** for every hug and smile you gave and for the beautiful painting gift. Thanks to **Dauren** for all the fantastic movie time. Thanks to **Erik** for your generous help with Matlab coding. Thanks to **Björn** for the nice talks during lunch and for the kindly help with insurance. Thanks to **Denis** for being a super cool friend and for the translations and guidance in Spain and Portugal. Thanks to **Agatha** and **Almir** for all the good music, good wine and good food. Many thanks to **Görel, Lennart and Per-Olof** for always saving me from problems. I admire everyone in TVRL for being in my life.

感谢我的父母，给予我生命，给予我经历这一切美好的可能。感谢你们无条件的支持，无条件的信任，无条件地接受我的一切。文字简短，感恩之情绵长，唯愿你们平安健康。Thanks to my parents for giving me life and the possibility to experience the wonderful world. Thank you for your unconditional support, trust, and acceptance of who I am. Text is too short to express the long gratitude. Wish you always safe and healthy.

感谢我的弟弟，幼时的陪伴，现在的呵护。希望你工作顺利，身体倍棒，可以独当一面，偶尔也可以放下一切，做无忧无虑的小孩。

感谢我的同学、朋友、丈夫——安冬。感谢你和我一起经历，有你的日子里没有黑暗，没有无聊，没有害怕。

感谢我的女儿，有你的每一天都让我觉得自己无比幸运。希望你无忧无虑，健康长大，妈妈爱你（此处有拥抱和亲亲）。

Papers

Appended papers

- I. **Du, Y.**, Berndtsson, R., An, D., Zhang, L., Hao, Z., & Yuan, F. (2017). Hydrologic response of climate change in the source region of the Yangtze River, based on water balance analysis. *Water (Switzerland)*, 9(2), [115].
- II. **Du, Y.**, Berndtsson, R., An, D., Zhang, L.T., Yuan, F., & Hao, Z. (2019). Integrated large - scale circulation impact on rainy season precipitation in the source region of the Yangtze River. *International Journal of Climatology*, [joc.6332].
- III. **Du, Y.**, Berndtsson, R., An, D., Zhang, L.T., Yuan, F., B. Uvo, C., & Hao, Z. (2019). Multi-space seasonal precipitation prediction model applied to the source region of the Yangtze River, China. *Water (Switzerland)*, 11(12), [2440].
- IV. **Du, Y.**, Berndtsson, R., An, D., & Ju, Q. (2020). Estimation of future precipitation over the source region of the Yangtze River, China, using NEX-GDDP dataset. (Manuscript).

Author's contribution to appended papers

Paper I. The first author collected data, designed the study, analyzed the results, and wrote the manuscript. The co-authors participated in discussion and helped to revise the manuscript.

Paper II. The first author collected data, planned the work, analyzed the results, and wrote the manuscript. The co-authors participated in discussion and helped to revise the manuscript.

Paper III. The first author collected data, designed the model, analyzed the results, and wrote the manuscript. The co-authors participated in discussion and helped to revise the manuscript.

Paper IV. The first author collected data, designed the study, analyzed the results, and wrote the manuscript. The co-authors participated in discussion and helped to revise the manuscript.

Related publications not included in this thesis:

Journal papers

- I. **Du, Y.** (2020). Can the wind in the Pacific Ocean influence the rainfall across the Himalaya mountains? (Popular science summary) VATTEN– Journal of Water Management and Research 76: 1. 2020.
- II. An, D., **Du, Y.**, Berndtsson, R., Niu, Z., Zhang, L.T., & Yuan, F. (2020). Evidence of climate shift for temperature and precipitation extremes across Gansu Province in China. Theoretical and Applied Climatology, 139(3-4), 1137-1149.
- III. Yuan, F., Liu, J., Berndtsson, R., Hao, Z., Cao, Q., Wang, H., **Du, Y.**, & An, D. (2020). Changes in precipitation extremes over the source region of the Yellow River and its relationship with teleconnection patterns. Water (Switzerland), 12(4), [978].

Conference abstracts

- I. Olsson, J., Sörensen, J., **Du, Y.**, An, D., Berg, P., Toivonen, E., and Belusic, D. (2020). Short-duration rainfall extremes in very high-resolution climate projections: historical evaluation and future projections, EGU General Assembly 2020, Online, 4–8 May 2020, EGU2020-7007.
- II. **Du, Y.**, Berndtsson, R. (2019). Integrated impacts of large-scale circulations on rainy season precipitation in the source region of Yangtze River. EGU General Assembly 2019, 7-12 April, in Vienna, Austria, EGU2019-2901.
- III. **Du, Y.**, Berndtsson, R., Zhang, L.T., An, D., Hao, Z., & Ju, Q. (2016). Spatial variation of precipitation in the Huang-Huai-Hai River Basin under climate change. Abstract from NORDIC WATER 2016 XXIX Nordic Hydrological Conference, Kaunas, Lithuania.
- IV. An, D., Zhang, L.T., Berndtsson, R., **Du, Y.**, Li, Z., & Yao, C. (2016). Application of different hydrologic models in flash floods simulation. Abstract from NORDIC WATER 2016 XXIX Nordic Hydrological Conference, Kaunas, Lithuania.

Abbreviations and symbols

ANN	Artificial Neural Network
BCSD	Bias Correction/Spatial Disaggregation
CMA	China Meteorological Administration
CMIP5	Coupled Model Intercomparison Project 5
COR/R	Pearson Correlation Coefficient
CPC	Climate Prediction Centre, USA
CPRCM	Convection-permitting Regional Climate Model
DMI	Dipole Mode Index
ENSO	El Niño Southern Oscillation
GCM	General Circulation Models
IOD	India Ocean Dipole
JAMSTEC	Japan Agency for Marine-Earth Science and Technology
MAE	Mean Average Error
MFC	Moisture Flux Convergence
MLR	Multiple Linear Regression
MME	Multi-Model Ensemble
MMet5	Multi-Model Ensemble of Top Five Models
NAO	North Atlantic Oscillation
NASA	National Aeronautics Space Administration
NCEP	National Centers for Environmental Prediction, USA
NEX-GDDP	NASA Earth Exchange Global Daily Downscaled Projections
NOAA	National Oceanic and Atmospheric Administration, USA
PC	Principal Component
PCA	Principal Component Analysis
PDO	Pacific Decadal Oscillation
PNA	Pacific/North American Pattern
POL	Polar/Eurasia Pattern
RCM	Regional Climate Models

RCP	Representative Concentration Pathways
Rho	Spearman's Rank Correlation
RI	Comprehensive Rating Index
RMSD	Root-Mean Square Difference
RMSE	Root-Mean Square Error
SCA	Scandinavia Pattern
SD	Standard Deviation
SOI	Southern Oscillation Index
SRTM	Shuttle Radar Topography Mission
SST	Sea Surface Temperature

List of figures

Figure 1. Structure of the thesis.....	2
Figure 2. Illustration of climate variability and climate change.	3
Figure 3. (a) Location of the source region of the Yangtze River; (b) topography and gauge locations	10
Figure 4. Flow chart of the PCA-ANN model.	19
Figure 5. Annual time series for water storage change (ΔW , 1957-2013) in the SRYR.....	24
Figure 6. (a) Mean annual precipitation of the source region of the Yangtze River, (b) Trend in mm per year during 1961-2015	24
Figure 7. Spatial pattern for mean seasonal precipitation and its trend in the SRYR during 1961-2015.....	25
Figure 8. Loadings of first two principal components for rainy season precipitation in SRYR	26
Figure 9. Spearman correlation between PCs of the rainy season precipitation in the SRYR and annual average SST: (a) PC1; (b) PC2.....	28
Figure 10. Time series of PC1 with inversed PDO index (solid line) and SOI index (broken line).	29
Figure 11. Precipitation anomalies under different scenarios	31
Figure 12. Composites of moisture flux at 500 mb with MFC under different scenarios	32
Figure 13. Pearson correlation between original and PCA-ANN simulated precipitation anomalies; (a) spring, (b) summer, (c) autumn, and (d) winter.	35
Figure 14. Taylor diagram of 21 individual NEX-GDDP models.	36
Figure 15. Rankings of 21 individual NEX-GDDP models for four stations.....	37
Figure 16. Comprehensive ranking index (RI) of 21 individual NEX-GDDP models for the basin	38
Figure 17. Annual precipitation change ratio in near- and far-future periods under RCP4.5 (blue) and RCP8.5 (red) scenarios from the multi-model ensemble (MME) mean with one inter-model standard deviation	39
Figure 18. Change ratios (%) using two different ensembles for annual precipitation (a,c) and summer precipitation (b,d) at each station under two different scenarios.....	40
Figure 19. Spatial distribution of precipitation change under RCP4.5 and RCP8.5 for near- and far-future period from MMEt5 ensemble	42

List of tables

Table 1. Summary of atmospheric circulation patterns considered in this study.	6
Table 2. Hydro-climatic stations used in the analysis.	11
Table 3. The 21 GCM models in NEX-GDDP dataset.	13
Table 4. Trend analysis for hydro-climatic variables in the SRYR.	23
Table 5. Positive (+) and negative (-) phases of PDO and SOI and combinations.....	29
Table 6. Explained variance of leading PCs for seasonal precipitation.	33
Table 7. Performance and structure of the predictive ANN model.....	34
Table 8. The top five models with best performance for each station and the whole basin.....	38

1.Introduction

An ecotone is a transition area where two biological communities meet and integrate. The source region of the Yangtze River (SRYR), the origin of the longest river in China, is one of the cold region ecotones, which faces considerable challenges: degraded grassland, endangered biodiversity, and frequent natural disasters. Topography in the source region is contrasting compared with the downstream basin as the average elevation is above 4500 m amsl (90°33'-95°20'E, 32°26'-35°46'N), and the area is covered with glaciers, permafrost, alpine grassland, and meadow, thus makes it a rigorous habitat for all lives. Moreover, due to the high elevation and low temperature in the region, a huge water volume is retained in glaciers, permafrost, and lakes. Therefore, water resources are fundamental for sustainable local ecosystem and secure downstream water supplies.

Over the past century, global climate has undergone a significant warming. The general warming of the Tibet Plateau during the past 50 years has been stronger than in other regions on the same latitude (Bibi et al., 2018, Yao et al., 2000). Precipitation shows great sensitivity to climate change and its variations bring considerable renewal to vegetation types, land cover, and species evolution, as it is an important medium of thermal exchange. Short-term variations and long-term imbalance of precipitation may affect the ecotone negatively. Therefore, adaptation strategies balancing economic, ecological, and social development are urgent tasks for the local government, which necessitate reliable scientific information of precipitation variation.

Based on this demand, a comprehensive investigation to access present and future variations of precipitation in this area is conducted. We firstly analyse historical climate change in a view of water balance. Then, precipitation variability and drivers of this variability are investigated by analysing relations with large-scale climate indices. An artificial neural network model is established to simulate seasonal precipitation variability using significantly related climate indices. Finally, we investigate future precipitation pattern under different emission scenarios. The findings of this study will benefit stakeholders and policymakers who need scientifically robust climate information to guide societal responses to changing climate.

Specific objectives of this study are (Figure 1):

to determine the state of art of research with respect to climate and water resources for the SRYR and investigate the water balance variation and historical hydroclimatic trend during the last 50 years (**Paper I**).

to identify the spatial and temporal variability of rainy season precipitation in the SRYR in relation to teleconnection patterns and access the integrated impact of the teleconnections (**Paper II**).

to quantify seasonal precipitation variability in the SRYR by simulating precipitation patterns using significantly correlated teleconnection indices (**Paper III**).

to investigate future precipitation change under different scenarios in the SRYR using high resolution NEX-GDDP dataset (**Paper VI**).

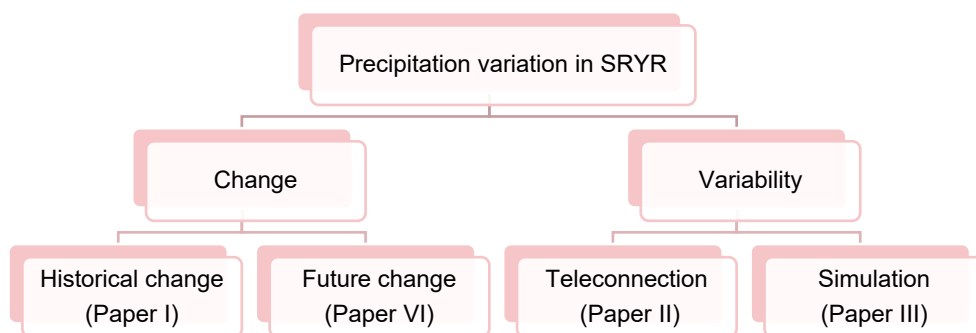


Figure 1. Structure of the thesis.

2. Theoretical background

2.1. Climate variability and climate change

When investigating the characteristics of regional climate, it is important to include both variability and change, which are different but intricately connected.

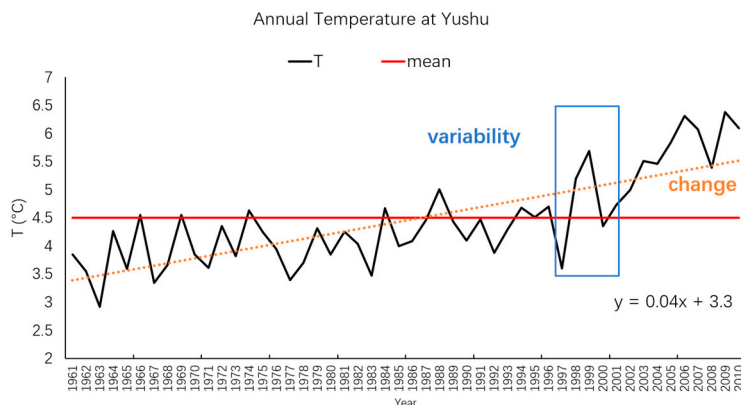


Figure 2. Illustration of climate variability and climate change.

Climate variability refers to a climatic variable of a region deviating from its long-term mean, which can be referred to as ‘anomalies’. Figure 2 shows that the average annual temperature at the Yushu station in the SRYR during 1961-2010 is 4.5°C . The interannual fluctuation around the long-term mean is referred to as variability. The time scale for investigating climate variability ranges from month to decades. Variability may result from natural internal processes within the local climate system or from variation in natural external forces, for example the atmospheric and oceanic circulation.

Climate change refers to alterations that occur over several decades to millennia. In Figure 2, the annual temperature at Yushu station presents an increasing trend over the period 1961-2010, with a slope of 0.4°C per decade, which is referred to as ‘climate change’. While climate change can be caused by natural processes at geological time scales, more concern is given to changes attributable to human activity such as the increase of greenhouse gas emissions. The Fifth Assessment Report from the Intergovernmental Panel on Climate Change (IPCC, 2013)

concluded that more than half of the observed increase in global average temperature is caused by elevated emission of carbon dioxide and other greenhouse gases.

2.2. Large-scale circulation patterns

Large-scale circulation patterns refer to atmospheric and oceanic circulation over different parts of the earth, caused by different heating mechanisms. The atmosphere and ocean jointly interact with each other by energy exchange, which triggers climate to vary at a seasonal or annual time scale. Large-scale circulation patterns are indices of climate variability. Important patterns that have impacts on global-scale climate are delineated in the below (**Table 1**).

2.2.1 El Niño Southern Oscillation (ENSO)

ENSO is a quasi-periodic climate pattern that occurs across the tropical Pacific Ocean and couples two processes: the warm oceanic phase (El Niño) accompanying high air surface pressure in the western Pacific and the cold phase (La Niña) accompanying low air surface pressure in the western Pacific (Ropelewski and Jones, 1987, Gong and Wang, 1999, Wang and Xu, 2018). The fluctuations in ocean temperatures during El Niño and La Niña are accompanied by even larger-scale fluctuations of the overlaying atmosphere, known as the Southern Oscillation. Sea Surface Temperature (SST) and the Southern Oscillation Index (SOI) are the most commonly used indicators to quantify the strength of an ENSO event (Chiew et al., 1998). SOI is measured by the difference in surface pressure anomalies between Tahiti and Darwin, Australia (Power and Kociuba, 2011). Prolonged periods of negative (positive) SOI values coincide with abnormally warm (cold) ocean waters across the eastern tropical Pacific typical of El Niño (La Niña) episodes. In warm ENSO years, anticyclone circulation may bring moisture to the Yangtze River basin, leading to above-normal rainfall (Ping et al., 2006, Cao et al., 2017).

2.2.2 Pacific Decadal Oscillation (PDO)

PDO is a Pacific climate variability pattern that usually shifts phase on a 20-30-year inter-decadal timescale (Trenberth and Hurrell, 1994, Mantua and Hare, 2002, Canedo-Rosso et al., 2019). It is detected as warm/cool surface water in the Pacific Ocean (north of 20°N). During a ‘warm’ or ‘positive’ phase, the western Pacific becomes cool and part of the eastern ocean warms while during a ‘cold’ or ‘negative’ phase, the opposite pattern occurs (Zhang et al., 1997, Mills and Walsh, 2013). Research has stated that precipitation over the Yangtze River basin decreases during

a warm PDO phase, and increases when the PDO enters a cold phase (Ouyang et al., 2014). Joint effects of ENSO and PDO will result in complex precipitation variability (Xiao et al., 2015).

2.2.3 North Atlantic Oscillation (NAO)

NAO is based on the surface sea-level pressure difference between the Subtropical (Azores) High and the Subpolar Low (Barnston and Livezey, 1987). The positive phase of the NAO reflects below-normal height and pressure across high latitudes of the North Atlantic and above-normal height and pressure over the central North Atlantic, eastern United States, and western Europe (Yuan, 2015). The negative phase reflects the opposite pattern of height and pressure anomalies over these regions. Both phases of the NAO are associated with basin-wide changes in the intensity and location of the North Atlantic jet stream and storm track, and in large-scale modulations of the normal patterns of zonal and meridional heat and moisture transport, which in turn results in changes in temperature and precipitation patterns often extending from eastern North America to western and central Europe (<https://www.ncdc.noaa.gov/teleconnections/nao/>).

2.2.4 Indian Ocean Dipole (IOD) and Dipole Mode Index (DMI)

Indian Ocean Dipole (IOD) is defined by opposite signs of sea surface temperature anomalies in the western tropical Indian Ocean and that in the eastern tropical Indian ocean (Saji and Yamagata, 2003). Intensity of the IOD is represented by anomalous SST gradient between the western equatorial Indian Ocean (50°E-70°E and 10°S-10°N) and the south eastern equatorial Indian Ocean (90°E-110°E and 10°S-0°N). This gradient is called Dipole Mode Index (DMI). During a positive IOD, above-warmer SSTs develop over tropical western Indian Ocean, and above-cooler SSTs develop over tropical eastern Indian Ocean. During a negative IOD, the opposite happens and results in westerly winds blowing toward the Indian subcontinent (Paul and Rashid, 2017).

2.2.5 Pacific/North American Pattern (PNA)

PNA pattern is one of the most prominent modes of low-frequency variability in the Northern Hemisphere extratropics (Barnston and Livezey, 1987). The PNA pattern reflects a quadrupole pattern of 500 millibar height anomalies of the similar sign located south of the Aleutian Islands and over the south-eastern United States. Anomalies with signs opposite to the Aleutian center are located in the vicinity of Hawaii, and over the intermountain region of North America (central Canada) during winter and fall (<https://www.ncdc.noaa.gov/teleconnections/pna/>). The PNA

pattern is associated with strong fluctuations in the strength and location of the East Asian jet stream. It is strongly influenced by the El Nino-Southern Oscillation phenomenon (<https://www.cpc.ncep.noaa.gov/data/teledoc/pna.shtml>).

2.2.6 Scandinavia Pattern (SCA)

The primary influence centre of SCA locates above the Scandinavian Peninsula, with two weaker centres of opposite sign, one over the western Europe and the other over eastern Russia/ western Mongolia (Barnston and Livezey, 1987, Bueh and Nakamura, 2007). Its positive phase is characterized by prominent anticyclone anomalies over Scandinavian Peninsula and western Russian, give above-normal precipitation across southern Europe, and dry conditions over the Scandinavian region (<https://www.cpc.ncep.noaa.gov/data/teledoc/scand.shtml>).

2.2.7 Polar/Eurasia Pattern (POL)

POL consists of two opposite height anomalies, one over the polar region and the other over northern China and Mongolia (Barnston and Livezey, 1987). This pattern is associated with fluctuations of the strength of the circumpolar circulation, with a positive phase reflecting an enhanced circumpolar vortex and a negative phase reflecting a weaker than average polar vortex. The POL is mainly associated with above average temperatures in eastern Siberia and below-average temperatures in eastern China and above average precipitation in the polar region of Scandinavia (<https://www.cpc.ncep.noaa.gov/data/teledoc/poleur.shtml>).

Table 1. Summary of atmospheric circulation patterns considered in this study.

Circulation pattern	Definition and center(s) of circulation	Reference
SOI	difference in surface air pressure between Tahiti and Darwin	Ropelewski and Jones (1987)
PDO	leading pattern under empirical orthogonal function analysis of sea surface temperature anomalies in the poleward of 20°N in North Pacific Ocean	Trenberth and Hurrell (1994)
NAO	pressure difference between Greenland and the central latitudes of the North Atlantic between 35°N and 40°N	Barnston and Livezey, 1987
DMI	anomalous sea surface temperature gradient between the western equatorial Indian Ocean (50°E-70°E and 10°S-10°N) and the south eastern equatorial Indian Ocean (90°E-110°E and 10°S-0°N)	Saji and Yamagata (2003)
PNA	a quadrupole pattern of 500 millibar height anomalies of similar sign located south of the Aleutian Islands and over the southeastern United States, opposite sign located in the vicinity of Hawaii, and over the intermountain region of North America	Barnston and Livezey 1987
SCA	primary center of influence above the Scandinavian Peninsula, with two other centers of action with the opposite sign, one over the north-eastern Atlantic and the other over central Siberia to the southwest of Lake Baikal	Bueh and Nakamura 2007
POL	opposite height anomalies over the polar region and the region of northern China and Mongolia	Barnston and Livezey 1987

2.3. General circulation models and NEX-GDDP dataset

To prepare for future climate change with more accurate information, increasingly advanced climate models are being developed over time. General Circulation Models (GCMs), representing physical processes in the atmosphere, ocean, cryosphere, and land surface, are currently indispensable tools that complement researchers for understanding the change of global climate system due to increasing greenhouse gas concentrations (https://www.ipcc-data.org/guidelines/pages/gcm_guide.html). Numerous studies have confirmed that GCMs can well simulate the main characteristics of global warming attributed by natural processes and anthropogenic effects. However, most GCMs run on grids of relatively coarse resolution, typically more than 100 km, which limits their ability to capture the spatial details of regions. This results in large biases for precipitation (Suzuki-Parker, 2012). In addition, the interacting influence of East Asian and South Asian monsoon, plus complex topography of the Tibet Plateau, add more restrictions for the application of GCMs on the Tibet Plateau (Su et al., 2013).

To overcome this limitation of GCMs, downscaling methods, including both statistical and dynamical procedures, are applied to obtain more refined precipitation patterns, reduce the simulation error of the models, and thus improve forecasting of future regional precipitation (Murphy, 1999, Knutson et al., 2013, Ekstrom et al., 2015). In June 2015, a high-resolution downscaled NASA Earth Exchange Global Daily Downscaled Projections (NEX-GDDP) dataset was released by the National Aeronautics and Space Administration of the United States (NASA), which statistically downscaled 21 GCMs from the Coupled Model Intercomparison Project 5 (CMIP5).

NEX-GDDP provides global-scale, high-resolution (spatial resolution: 0.25° longitude \times 0.25° latitude) data and corrects the deviation of future estimates, which provides possibilities to improve the simulation and projection of precipitation at a regional scale. The NEX-GDDP dataset is produced using results from downscaled climate models under two of the four greenhouse gas emission scenarios known as Representative Concentration Pathways (RCPs) (Meinshausen et al., 2011), which are derived from the GCM runs conducted under CMIP5 (Taylor et al., 2012). The dataset was provided to promote scientific research at regional scales and enhance public understanding about future climate change.

To generate the NEX-GDDP dataset, two steps are conducted: first, biases of the CMIP5 model data are corrected by comparing with observation data; secondly, high-resolution model data is obtained through the Bias Correction/Spatial Disaggregation (BCSD) method, which is specifically designed to address some limitations of current GCMs' outputs (Maurer and Hidalgo, 2008, Wood et al., 2004, Thrasher et al., 2012). For more information on the dataset, see <https://nex.nasa.gov/nex/projects/1356/>.

After its release, the NEX-GDDP dataset was applied to study the near- and long-term climate, and proved robust, even in regions with complex topography. Compared with raw CMIP5 model data, NEX-GDDP can provide more detailed information at regional scales on climate change, and the biases of model simulation results are greatly reduced. Previous findings suggest that NEX-GDDP is consistent with historical observations at the monthly scale (Raghavan et al., 2018, Jain et al., 2019, Bao and Wen, 2017).

3. Study area

The Yangtze River (Changjiang River) is the longest river in Asia and the third longest river in the world, with a length of 6380 km. The source region of the Yangtze River (SRYR) refers to the area upstream of Zhimenda runoff station (Figure 3) located in the hinterland of the Qinghai-Tibet plateau. The topography of the source region contrasts the downstream basin as the average elevation is above 4500 m amsl (90°33'-95°20'E, 32°26'-35°46'N), with an area of approximately $13.77 \times 10^4 \text{ km}^2$ covered with glaciers, permafrost, alpine grassland, and meadow.

Over the past century, global climate has undergone a significant warming. The average warming in the Tibet Plateau during the past 50 years has been stronger than in other regions on the same latitude (Yao et al., 2000). Consequences of climate change on ecotones like the SRYR will be tremendous because they are fragile and less stable than other ecosystems. Long-term continuous change of water resources together with short-term fluctuant variabilities emphasize the need of scientific support for water resources management and ecosystem protection.

Meanwhile, the monsoon circulation in the SRYR is different from other parts of the basin due to the attenuation of the East Asian monsoon at high altitudes and large distance from the ocean. Previous studies on water vapor origin have identified the SRYR as a transition zone, suggesting shifting influences between the westerlies and the Indian monsoon (Yao et al., 2013, Zhang et al., 2016), which gives rise to a complex precipitation pattern in terms of spatial and temporal variation. The full understanding of this complexity is yet to be addressed. Thus, further research is needed to resolve influencing mechanisms for precipitation variability in this area.

The SRYR consists of three sub-basins, namely Chumar (north source), Tuotuohe (middle source), and Dangqu (south source) River. These three sub-basins collect more than 200 smaller river tributaries that discharge from Zhimenda into the lower section. Due to the harsh climatic conditions, only about 15,000 people live in the area (0.09 person per km^2). Thus, the river system is mainly pristine. As a result, the direct human impact on the hydrological processes is small. Based on Köppen Geiger climate classification system (Peel et al., 2007), the SRYR is characterized by a monsoon-influenced subarctic climate (Dwc), which means dry winters and cool summers.

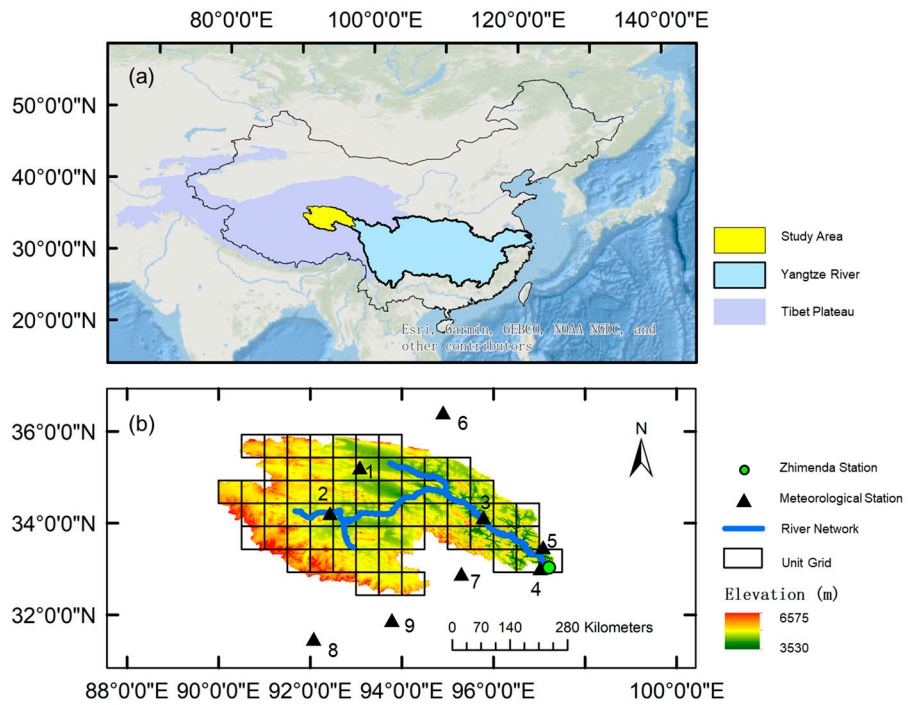


Figure 3. (a) Location of the source region of the Yangtze River; (b) topography and gauge locations. The 9 meteorological stations are represented with black triangles (Paper I and Paper IV). The Zhimenda hydrological station is represented with green circle. The unit grid of interpolated precipitation dataset is shown with black squares (Paper II and Paper III).

4. Data

4.1. Climate variables

Monthly observed temperature and precipitation were obtained from the data-sharing website of National Meteorological Information Center, China (<http://data.cma.cn/>). In total, 4 stations inside (Station No.1-4, Table 2) and 5 stations outside (Station No.5-9, Table 2) the catchment boundary were used to analyse the trend of water balance components during 1957-2015 (**Paper I**). Monthly discharge data of Zhimenda hydrological station (Station No.10, Table 2) from Yangtze River Conservancy Commission, China, was used to determine runoff from the SRYR (1957-2013). Detailed information of the stations used are listed in Table 2 and locations are depicted in Figure 3.

To access model performances of NEX-GDDP dataset and investigate future pattern on monthly precipitation in the SRYR, stations inside the study area (Station No. 1 to No. 4) were selected (**Paper IV**).

Table 2. Hydro-climatic stations used in the analysis.

Station		Longitude (° E)	Latitude (°N)	Elevation (m)	Mean annual temp. (°C/year)	Mean annual precip. (mm/year)
1	Wudaoliang	93.08	35.22	4612	-5.2	290.8
2	Tuotuohe	92.43	34.22	4533	-3.9	292.3
3	Qumalai	95.78	34.13	4175	-2.0	414.7
4	Yushu	97.02	33.02	3717	3.4	488.8
5	Qingshuihe	97.08	33.48	4415	-4.5	518.2
6	Geermu	94.90	36.42	2808	5.2	42.1
7	Zaduo	95.30	32.90	4066	0.7	359.1
8	Naqu	92.07	31.48	4507	-1.1	292.7
9	Suoxian	93.78	31.89	4023	1.9	381.4
10	Zhimenda	97.22	33.03		-2.9 (Basin Average)	327.4 (Basin Average)

Monthly gridded precipitation data ($0.5^{\circ} \times 0.5^{\circ}$) for the period 1961-2016 over the SRYR were obtained from the China Meteorological Administration (CMA) (**Paper**

II, Paper III, depicted in Figure 3). Regular grid points were interpolated by CMA based on observed precipitation data and a Digital Elevation Model from GTOPO30 (Hutchinson, 1998). This dataset has been widely used in climate analysis, numerical model verification, and hydrological studies (Shi et al., 2017, Wang et al., 2017).

To interpret the spatial distribution of climate variables, topography information of The Shuttle Radar Topography Mission (SRTM) 90 m digital elevation data (Figure 3) were downloaded from the Consortium for Spatial Information under Consultative Group on International Agricultural Research (CGIAR-CSI).

4.2. Large-scale circulation

Monthly global sea surface temperature (SST) data ($1^\circ \times 1^\circ$), version HadISST 1.1 (Rayner et al., 2003), were obtained from the British Atmospheric Data Centre (online at <https://www.metoffice.gov.uk/hadobs/hadisst/>, **Paper II**). As HadISST1 can capture trends in global, hemispheric, and regional SST, it is widely used in studies of the large-scale signals associated with interannual to decadal climate variability (Chelton and Risien, Zhang et al., 2018).

To describe modes of atmospheric circulation, this study considers six climate indices influencing climate variability over the Northern Hemisphere and especially China: Southern Oscillation Index (SOI), Pacific Decadal Oscillation (PDO), North Atlantic Oscillation (NAO), Pacific/North American (PNA) Pattern, Scandinavia Pattern (SCA), (**Paper II** and **Paper III**) and Polar/Eurasia Pattern (POL) (**Paper III**). Standardized monthly data of climate indices are available from the Climate Prediction Centre (CPC) at the National Weather Service of the United States (<http://www.cpc.ncep.noaa.gov/data/teledoc/telecontents.shtml>) and Dipole Mode Index (DMI) from Japan Agency for Marine-Earth Science and Technology (JAMSTEC). Further explanation of each climate index is described by Barnston and Livezey (1987) and Washington et al. (2000).

4.3. Reanalysis data

Monthly atmospheric reanalysis data were obtained from NCEP (National Centers for Environmental Prediction of the United States) dataset (Kalnay et al., 1996) provided by National Oceanic and Atmospheric Administration of the United States (NOAA) at a horizontal resolution of $2.5^\circ \times 2.5^\circ$, and vertical layers from 1000 to 10 millibar. Physical variables used in this study are specific humidity, meridional, zonal wind components, and pressure (**Paper II**).

4.4. NEX-GDDP dataset

Daily precipitation data were obtained at each grid ($0.25^\circ \times 0.25^\circ$) covering the four observation stations, for the period 1961–2005 (historical period), and future projection 2041–2060 (near-future period), and 2081–2100 (far-future period) under RCP4.5 and RCP8.5 scenarios (**Paper IV**). The scenarios include the historical experiment and the RCP 4.5 and 8.5 experiments developed for the Fifth Assessment Report of the Intergovernmental Panel on Climate Change (IPCC AR5). Table 3 shows the 21 GCM models that were downscaled to obtain the NEX-GDDP dataset.

Table 3. The 21 GCM models in NEX-GDDP dataset.

No.	Model	Country	Institution
1	ACCESS1-0	Australia	Commonwealth Scientific and Industrial Research Organization
2	BNU-ESM	China	College of Global Change and Earth System Science, Beijing Normal University
3	CCSM4	USA	National Center of Atmospheric Research
4	CESM1-BGC		
5	CNRM-CM5	France	National Centre of Meteorological Research
6	CSIRO-Mk3-6-0	Australia	Commonwealth Scientific and Industrial Research Organization/Queensland Climate Change Centre of Excellence
7	CanESM2	Canada	Canadian Centre for Climate Modelling and Analysis
8	GFDL-CM3	USA	NOAA Geophysical Fluid Dynamics Laboratory
9	GFDL-ESM2G		
10	GFDL-ESM2M		
11	IPSL-CM5A-LR	France	Institute of Pierre-Simon Laplace
12	IPSL-CM5A-MR		
13	MIROC-ESM	Japan	Atmosphere and Ocean Research Institute (The University of Tokyo), National Institute for Environmental Studies, and Japan Agency for Marine-Earth Science and Technology
14	MIROC-ESM-CHEM		
15	MIROC5		
16	MPI-ESM-LR	Germany	The Max Planck Institute for Meteorology
17	MPI-ESM-MR		
18	MRI-CGCM3	Japan	Meteorological Research Institute, Japan
19	NorESM1-M	Norway	Norwegian Climate Center, Norway
20	BCC-CSM1-1	China	Beijing Climate Center, China Meteorological Administration
21	INMCM4	Russia	Institute for Numerical Mathematics

5. Methods

5.1. Statistical analysis

Mann-Kendall Trend Test

The Mann Kendall Trend Test (M-K test) is a non-parametric test to analyse data for monotonic trends. The Kendall statistic was originally devised as a non-parametric test for trend by Mann (1945). Later Kendall (1975) derived the exact distribution of the test statistic. The method is a robust method for trend identification and has been widely used in hydrometeorological analysis. In this test, the null hypothesis (H_0) is that there is no trend in the data series over time; the alternate hypothesis (H_1) is that there is a trend (increasing or decreasing) over time. Statistical significance of the trend is evaluated at the 0.05 level of significance. A detailed procedure for this statistical test can be found in Burn and Hag Elnur (2002). Time series of different climatic variables in the SRYR were examined using the Mann-Kendall test (**Paper I, II, and III**).

Pearson Correlation

Pearson correlation coefficient was used to measure correlation between climate variables (**Paper I and Paper II**), and also to verify the performance of models against observations (**Paper III and Paper IV**). Pearson correlation (COR) is a statistic that measures linear correlation between two variables, which ranges between +1 and -1. A value of +1 is total positive linear correlation, 0 is no linear correlation, and -1 is total negative linear correlation. It was developed by Pearson (1895), and for which the mathematical formula is,

$$COR = \frac{\sum_{i=1}^n (x_i - \bar{x})(y_i - \bar{y})}{\sqrt{\sum_{i=1}^n (x_i - \bar{x})^2} \sqrt{\sum_{i=1}^n (y_i - \bar{y})^2}}, \quad (\text{Eqn. 1})$$

where x, y are the two variables, n is the number of attributes.

Spearman Correlation Analysis

Spearman's rank correlation (rho) (Myers and Well, 2003) is defined as the Pearson correlation coefficient between the rank variables. It is used to identify the relationships between precipitation and climate indices as it assumes no normality

or other specific distribution function for the variables. In this thesis, Spearman's rank correlation was used for correlation between precipitation anomalies and large scale circulation patterns to investigate the influencing indices for the studied basin (**Paper II and III**).

Principal Component Analysis

Principal component analysis (PCA) was used to find relationships between precipitation in the SRYR and teleconnection patterns using climate indices (**Paper II and III**).

Principal Component Analysis (PCA) presents complex data in a simplified way to identify relations between main governing variables (Uvo, 2003, Rana et al., 2012). The R mode PCA (Gocic and Trajkovic, 2014, Fazel et al., 2017), based on the covariance matrix of precipitation data, was used to produce new dataset with less variables by its eigenvectors. The loadings of PCA modes reveal the spatial patterns of its associated scores, also referred to as principal components (PCs), which provide information of their temporal variability. Mathematically, the transformation is defined by a set of loadings in U that map each row of X to a new vector of PCs in Z , given by $Z = XU$. And $z_1 = XU_1$ is the linear combination of elements in X that retains the greatest variance; $z_2 = XU_2$ is the linear combination that retains the greatest variance and is orthogonal with z_1 . In such way, individual variables of Z inherit the maximum possible variance from X . The number of PCs in Z is selected to be less than variable numbers in X to reduce dimensionality, which was decided based on a scree plot in this study.

5.2. Water balance and uncertainty

In hydrology, the water balance equation is used to describe the flow of water in and out of a system. A system can be one of several hydrological domains, such as a column of soil or a drainage basin.

Monthly water balances in the SRYR were calculated according to:

$$P_m - ETa_m - R_m = \Delta W_m, \quad (\text{Eqn. 2})$$

where P_m = monthly precipitation, ETa_m = monthly actual evapotranspiration, R_m = monthly runoff depth, and ΔW_m = monthly change in total water storage. Annual water storage change ΔW was calculated by summarizing monthly water storage change (**Paper I**).

As ETa_m is an important but non-observed variable in Eqn.2, temperature and precipitation data were used to calculate ETa_m by use of the Takahashi equation (Takahashi and Wang, 1979):

$$ETa_m = f(P_m, T_m) = \frac{3100P_m}{A+B*P_m^2 \exp(-\frac{34.4T_m}{235+T_m})}, \quad (\text{Eqn. 3})$$

$$ETa = \sum_{m=1}^{12} ETa_m, \quad (\text{Eqn. 4})$$

where ETa = annual actual evapotranspiration (mm), T_m = mean monthly temperature ($^{\circ}\text{C}$), ETa_m and P_m are the same as Eqn.2. A , B = parameters that depend on local meteorological and hydrological conditions. Eqns. (3)-(4) have previously been tested in the SRYR (Zhang et al., 2006, Qian et al., 2014) and A and B were determined to 3100 and 0.55 by wavelet and water balance analysis.

To estimate errors caused by the calculation, we quantified uncertainties for each component in the long-term water balance. Standard deviation (SD, Eqn.5) and average were both calculated using a 10-year moving average window (Karlsson et al., 2012). The upper (lower) range of the examined component was analysed by adding (subtracting) the moving standard deviation to (from) the moving average values respectively.

Standard deviation (SD) of monthly temperature (SD_{Tm}), precipitation (SD_{Pm}), and runoff (SD_{Rm}) are calculated as,

$$SD = \sqrt{\frac{\sum_{i=1}^n (x_i - \bar{x})^2}{n}}, \quad (\text{Eqn. 5})$$

where x is the variable, n is the number of attributes.

Since water storage change is dependent on temperature, precipitation and runoff, the standard deviations of annual water storage change ($SD_{\Delta W}$) were propagated from the independent variables as below,

$$SD_{Eta_m} = \sqrt{(\frac{\partial f}{\partial T_m})^2 SD_{Tm}^2 + (\frac{\partial f}{\partial P_m})^2 SD_{Pm}^2}, \quad (\text{Eqn. 6})$$

$$SD_{\Delta Wm} = \sqrt{SD_{Eta_m}^2 + SD_{Pm}^2 + SD_{Rm}^2}, \quad (\text{Eqn. 7})$$

$$SD_{\Delta W} = \sqrt{\sum_{m=1}^{12} SD_{\Delta Wm}^2}, \quad (\text{Eqn. 8})$$

where SD_{Eta_m} is the standard deviation of ETa_m , $SD_{\Delta Wm}$ is the standard deviation of ΔW_m , and m is the m^{th} month.

5.3. Water moisture convergence

Moisture advection is the horizontal transport of water vapor by wind. Measurement and knowledge of atmospheric water vapor, or ‘moisture’, is crucial to the prediction of weather elements, especially precipitation. Regions of moisture advection are often co-located with regions of warm advection.

To investigate the circulation mechanisms behind the variation in rainy season precipitation over the SRYR, several circulation terms were analyzed (**Paper II**). Moisture flux $q \cdot \bar{V}$ at surface layer was used to explore the circulation pattern (q is specific humidity; \bar{V} is horizontal wind vector).

Horizontal moisture flux convergence (MFC), also referred as negative moisture flux divergence (Banacos and Schultz, 2005), was selected to explore the possible vertical movement of moisture. MFC can be written as,

$$MFC = -\nabla \cdot (q \cdot \bar{V}) = -\bar{V} \cdot \nabla q - q \nabla \cdot \bar{V}, \quad (\text{Eqn. 9})$$

The elevation of SRYR is between 3530 to 6575 m, and most parts of the basin are lower than 5500 m except the mountain peak area. Therefore, 500 mb (5500 m) was selected as the surface layer. Moisture flux and MFC at 500 mb were calculated and compared for different circulation scenarios. To avoid biases of the composites results from the long-term trend, the wind vector and specific humidity series were first detrended before calculation for composite analysis.

5.4. Simulation model using large-scale circulation patterns

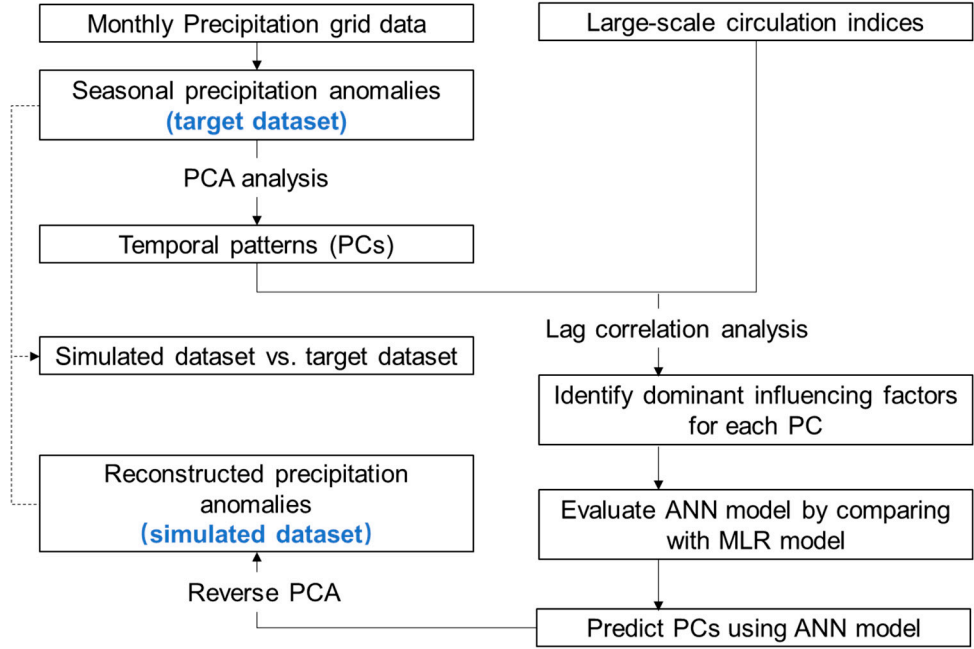


Figure 4. Flow chart of the PCA-ANN model.

To simulate precipitation pattern using large-scale circulation indices, a PCA-ANN model was established in **Paper III**. PCA-ANN model is a combination of Principal Component Analysis (PCA) and Artificial Neural Network (ANN), by which principal components (PCs) of the original precipitation dataset are used as simulating targets for the ANN model instead of using the original dataset. The step-by-step design of PCA-ANN model is shown in Figure 4.

ANN was used to map the qualified predictors (input) and predictable components (output). ANN customary architecture is composed of three layers of neurons: input, hidden, and output layer (Haykin, 1994). Development of an ANN model consists of the following procedure: (1) setting up a typical feed-forward neural network as this has been shown to be computationally superior in comparison to other alternatives (Hornik et al., 1989); (2) rescaling all input and output variables to (-1, 1) using,

$$x = \frac{2(x-x_{\min})}{(x_{\max}-x_{\min})} - 1, \quad (\text{Eqn. 10})$$

where x is the variable, x_{min} is the variable minimum, and x_{max} is the variable maximum;

(3) dividing the dataset into training, validation, and test sets (training set = fit ANN model weights, validation = select model type that provides the best level of generalization, and test set = evaluate the chosen model against the remaining data); (4) selecting the activation function to hidden and output layer and training algorithm that provide best fit to data; (5) identifying optimal number of neurons in the hidden layer by using a trial and error procedure by varying the number of hidden neurons from 2 to 10; (6) evaluating the ANN model with statistics for multi-criteria assessment, using mean absolute error (MAE, Eqn. 11), root mean squared error (RMSE, Eqn. 12), and Pearson correlation between observations and simulation results (COR, Eqn. 1). ANN analyses were performed using MATLAB Neural Network Toolbox,

$$MAE = \frac{\sum_{i=1}^n |(x_i - y_i)|}{n}, \quad (\text{Eqn. 11})$$

where x, y are the two variables, n is the number of attributes.

$$RMSE = \sqrt{\frac{\sum_{i=1}^n (x_i - y_i)^2}{n}}, \quad (\text{Eqn. 12})$$

where x, y are the two variables, n is the number of attributes.

The output from the ANN model can be transferred to precipitation anomalies through the inverse transform of rescaled and reconstructed PCs. The results yield a simulated precipitation dataset over the SRYR corresponding to 64 grid points.

When comparing performance between ANN and traditional multiple linear regression (MLR) models, a three-fold cross-validation technique was used (**Paper III**). All samples were randomly divided into three complementary subsets: $k_1=18$, $k_2=18$, $k_3=19$. For each unique subset: this subset was taken as a test set while the remaining two subsets were taken as training set; a model was trained on the training set and evaluated for the test set; the evaluation scores (MAE, RMSE, and COR) were retained, and the model discarded. To reduce variability, the evaluation results were averaged over the three rounds to give an estimate of the model's predictive performance. By comparing the performance, the best model was selected between ANN and MLR models, which was ANN in this study. Then, the ANN model was trained over the entire dataset to tune to a prediction model. Prediction results were compared to the target dataset using MAE, RMSE, and COR.

5.5. Future precipitation pattern using NEX-GDDP dataset

5.5.1. Performance evaluation of NEX-GDDP dataset

5.5.1.1 Taylor Diagram

To investigate the performance of NEX-GDDP dataset in the SRYR, the performance of each NEX-GDDP model was compared against observations by examining statistical metrics using the Taylor diagram (Taylor, 2001) in **Paper IV**. The diagram provides a summary of the model's performance in simulating the spatial pattern of different variables in terms of their Pearson correlation (COR, Eqn. 1), the standard deviation (SD, Eqn. 5), and root-mean-square difference (RMSD, same as RMSE, Eqn. 12).

The correlation is shown along a circular axis, which improves as a model is located closer to observation on the x-axis. The COR is the quantity that measures the degree of phase agreement of two fields. The SD of observation is taken as the center point, while the SD of each model is shown in terms of its distance from the observation. Similarly, the RMSD of each model is shown as the distance from the observations on the x-axis. The RMSD is the quantity that measures the degree of agreement in amplitude. The Taylor diagram was computed for the four grids by evaluating all 21 models of NEX-GDDP data for monthly precipitation against the observed in situ data.

5.5.1.2 Comprehensive rating index (RI)

On the basis of their statistical metrics, ranking among the models can be conducted (**Paper IV**). An overall ranking considering all evaluating indices can be obtained with a comprehensive rating index RI (Jiang et al., 2015), which is defined as,

$$RI = 1 - \frac{1}{nm} \sum_{i=1}^n rank_i, \quad (\text{Eqn. 13})$$

where m is the number of models (21 in this study), and n is the number of evaluating indices (3 in this study). Rank_i represents the rank number of each model, where the best-performing model is 1, and the worst model is 21. Therefore, the closer to 1 the value of RI is, the better the simulation is.

Based on this rating index, top five better performing models for each station were selected.

5.5.2 Multi-model ensemble

Multi-model ensemble is a widely used technique in climate studies and its advantage has been demonstrated in many studies (Wang et al., 2018, Weigel et al., 2008). Two multi-model ensembles were established in **Paper IV**. The first ensemble is the multi-model ensemble for all models (MME) in the NEX-GDDP dataset, by taking the average precipitation of all models at corresponding time interval. The second ensemble is, instead of taking the average of all models, only the top five best performing models are used (MMEt5). Equal weights are given to each model in both ensemble methods.

5.5.3 Bias correction

The linear scaling (LS) method aims to perfectly match the long-term monthly mean of corrected values with observed values (Lenderink, Buishand and van Deursen, 2007; Mendez et al., 2020). Precipitation is typically adjusted with a multiplier factor. The LS method operates with monthly correction values based on the differences between observations and model data in the historical period, which is 1961-2005 in this study (**Paper IV**),

$$P_{model}^{bc}(j) = P_{model}(j) \cdot \frac{\sum_{i=1}^n P_{obs}(j)}{\sum_{i=1}^n P_{model}(j)}, \quad (\text{Eqn. 14})$$

where P_{obs} , P_{model} are the monthly precipitation of observed and model data, n is the number of attributes, j represents the j^{th} month.

Future precipitation of ensembled models is bias corrected on monthly scale.

5.5.4 Future precipitation change

Projected rainfall is compared with observed rainfall and the spatial and temporal change is computed for the near-future (2041-2060) and far-future (2081–2100) periods for RCP 4.5 and 8.5 separately, taking 1986 to 2005 as the historical base line. The Delta method was applied to project future precipitation changes (**Paper IV**). The changes were calculated as,

$$c = \frac{P_f}{P_h} - 1, \quad (\text{Eqn. 15})$$

where P_f and P_h are the mean precipitation of the future and historical NEX-GDDP outputs.

6. Results and discussion

6.1. Historical climate change

6.1.1. Trend analysis on basin scale

The annual trends of hydroclimatic variables were analysed in **Paper I**. Table 4 shows the changing gradients and results of the Mann-Kendall test for all investigated variables. Long-term trends for temperature and precipitation are statistically significant with an increase of 0.34°C and 11.4 mm per decade. The runoff shows a small decadal increase by 3.3 mm, which is not statistically significant. Similar warming trend in SRYR has been revealed by several researchers (Zhang et al., 2008, Yao et al., 2014), which together confirms a significant warming in this area as it doubles the average increase rate of global temperature (0.18°C per decade, NOAA (2020)). A statistically insignificant trend for annual runoff during 1960-2009 has also been previously confirmed (Xie et al., 2003, Liang et al., 2011, Li et al., 2013).

Table 4. Trend analysis for hydro-climatic variables in the SRYR.

	Temperature	Precipitation	Runoff	Evapotranspiration	Change in water storage
	°C/decade	mm/decade	mm/decade	mm/decade	mm/decade
Gradient	0.34	11.4	3.3	7.6	-1.1
MK Sig.	0.000*	0.004*	0.077	0.000*	0.156

* denotes statistically significant at 0.05, 0.000 refers to significant level <0.001.

6.1.2. Water balance and uncertainty analysis

Annual actual evapotranspiration and corresponding annual water storage change were calculated and analysed in **Paper I**. For the actual evapotranspiration there is a clear positive and statistically significant trend of 7.6 mm per decade during 1957-2015 (Table 4). The basin scale water storage change, on the other hand, shows an insignificant negative trend (MK sig. 0.156 > 0.05, Table 4). The 10-year moving average for water storage change (ΔW) is generally below zero, which indicates potential loss of water storage in the study area (Figure 5). However, considering

the uncertainty boundaries, the water storage ranges approximately around zero and is occasionally positive. To summarize, the basin as a whole does not display a significant loss of water storage even if the ten-year average basin-scale water balance indicates a continuous small negative value since about 1980. In this case, the increase of calculated evapotranspiration derived from significantly increasing temperature, together with an increase in precipitation, leads to a relatively stable water storage during the study period. Meanwhile, the increasing of precipitation and evapotranspiration also suggest an accelerating water cycle in the SRYR.

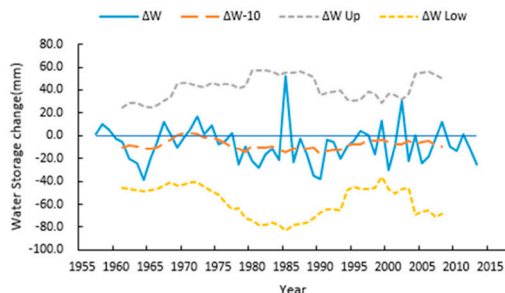


Figure 5. Annual time series for water storage change (ΔW , 1957-2013) in the SRYR; solid line denotes the annual time series, long dash line denotes 10-year moving average, and short dash lines denote the upper and lower boundaries propagated from temperature, precipitation and runoff time series.

6.1.3. Spatial pattern

Located on the Tibet Plateau, the SRYR precipitation shows high topographical dependence (**Paper III**). The mean annual precipitation varies markedly over the basin, with in general larger precipitation in the southeastern areas that decreases towards the northwestern high elevation areas (from 632.6 to 234.6 mm). This distribution stems from the southeasterly water vapor transfer that weakens as it approaches the inland. There is a significantly ($p < 0.05$) increasing trend in annual precipitation (warming) across the western part (Figure 6b). This trend equals about 2.3 mm/year for the significant area of the basin.

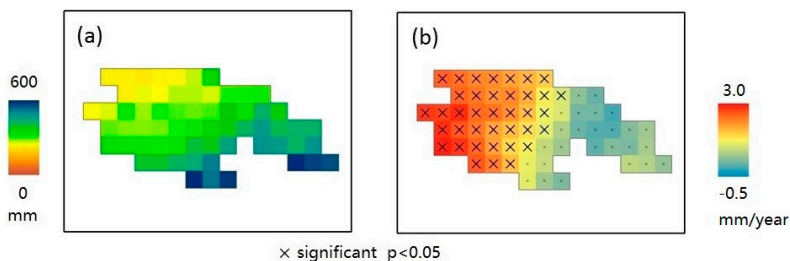


Figure 6. (a) Mean annual precipitation of the source region of the Yangtze River, (b) Trend in mm per year during 1961-2015, significant area ($p < 0.05$) represented by bold cross.

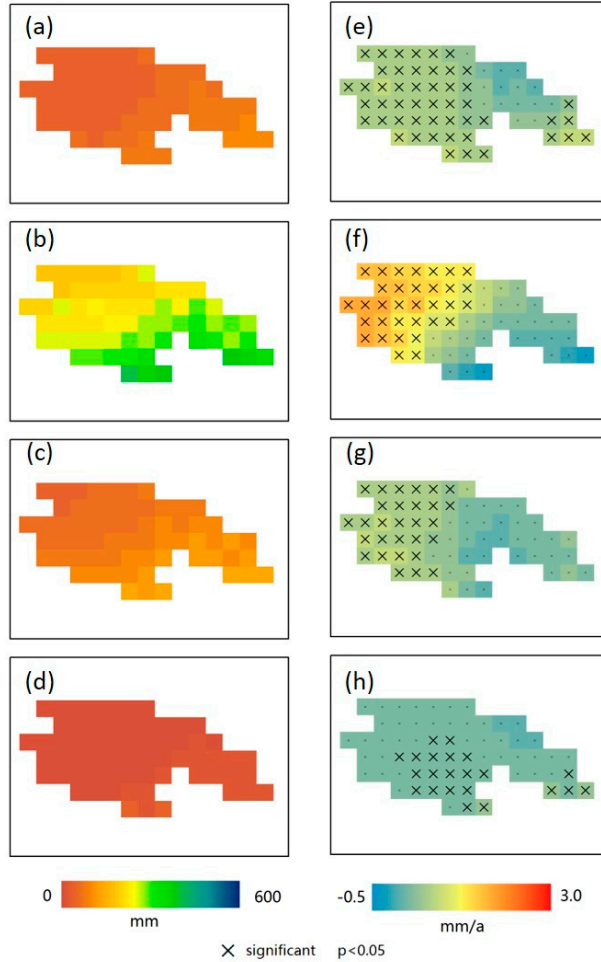


Figure 7. Spatial pattern for mean seasonal precipitation and its trend in the SRYR during 1961-2015. (a,e) spring (MAM), (b,f) summer (JJA), (c,g) autumn (SON), and (d,h) winter (DJF), significant area ($p < 0.05$) represented by bold cross.

Spatial pattern and temporal trend for seasonal precipitation were investigated in **Paper III**. Mean seasonal precipitation has an average range of 26.4 to 95.1 mm for spring (Figure 7a), 166.4 to 405.7 mm for summer (Figure 7b), 37.0 to 136.6 mm for autumn (Figure 7c), and 3.7 to 23.8 mm for winter (Figure 7d). In general, the largest precipitation for all seasons is observed over the south and southeast part of SRYR, while the driest areas are located in the northwestern parts. The seasonal precipitation for SRYR shows a remarkably high variability during the study period (1961-2015).

Trend analysis of seasonal mean precipitation shows both increasing and decreasing tendencies, but only the increasing trend is statistically significant ($p < 0.05$). The significantly ($p < 0.05$) increasing trend in spring (Figure 7e) ranges from 0.3 to 0.7 mm per year and occurs over the western parts and in the eastern periphery. During summer (Figure 7f), a statistically significant increasing trend ($p < 0.05$) only occurs over the western part, in the range of 0.8 to 1.9 mm per year. Autumn (Figure 7g) mean precipitation also shows a significant increase over the western part but with a smaller area than in summer. The general range of significantly increasing trend in autumn precipitation is between 0.3 and 0.7 mm per year. For winter (Figure 7h), mean precipitation displays significantly increasing trend (range 0.1 to 0.8 mm per year) over the central area and a small area in the southeast.

Focusing on rainy season precipitation (June, July, and August), PCA was applied to extract main spatial and temporal patterns for the gridded precipitation dataset (**Paper II**). Time series of the 64 grids covering the basin for rainy season precipitation anomalies were subjected to PCA. The first two principal components (PCs) were retained for further analysis, explaining 64.2% and 20.1% (cumulative variance 86.3%) of total variance, respectively. Loadings of the first two leading PCs were generated to identify the rainy season precipitation patterns (Figure 8). As shown in Figure 8, all PC1 loadings are positive, indicating a common variation in rainy season precipitation throughout the entire basin. The loading has a maximum in the central basin and decreases from this point. PC2 loadings include both positive and negative values. The zero isoline, aligned along the center, divides the basin into a west-east anti-phase pattern in response to rainy season precipitation variability. This is an influence of the westerlies and Indian monsoon from different directions (Yao et al., 2013, Zhang et al., 2016).

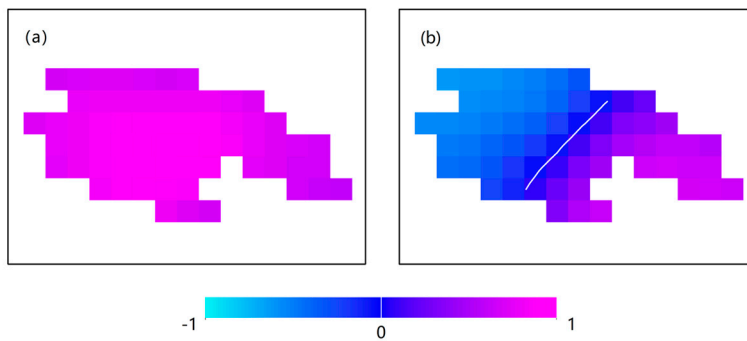


Figure 8. Loadings of first two principal components for rainy season precipitation in SRYR; (a) first PC; (b) second PC; white line denotes the zero isoline between positive and negative loadings.

6.2. Precipitation variability using teleconnections

6.2.1. Correlation with large-scale circulation pattern

To identify the SST areas that relate to rainy season precipitation variation in the SRYR, Spearman correlation between scores of the PCs and annual average SST was computed (**Paper II**). According to Figure 9, PC1 correlates with SST anomalies over the northern Atlantic Ocean, northern and eastern Pacific Ocean, and subtropical eastern Pacific Ocean. PC2 correlates mainly with Indian Ocean and eastern subtropical Pacific Ocean. Correlation with climate indices further verifies these associations. PC1 shows significant anti-phase correlation with PDO index ($\rho = -0.325$) and in-phase correlation with SOI index ($\rho = 0.261$), which are consistent with the correlated area of SST. This confirms the results by Su and Wang (2007), Tian et al. (2016), and Yuan et al. (2015) over the neighboring areas of Tibet Plateau regarding the influence of ENSO and PDO on precipitation.

Associations are further visualized in Figure 10, as PC1 shows consistency with inversed PDO index and SOI index. The SST anomaly correlation map and the significant correlation between the corresponding PC and climate indices imply that the first leading mode of the rainy season precipitation is associated with PDO and SOI. PC2 does not display significant correlation with the corresponding climate indices. Consequently, the conclusion is that the association between the second leading mode of the rainy season precipitation and large-scale circulation is not significant.

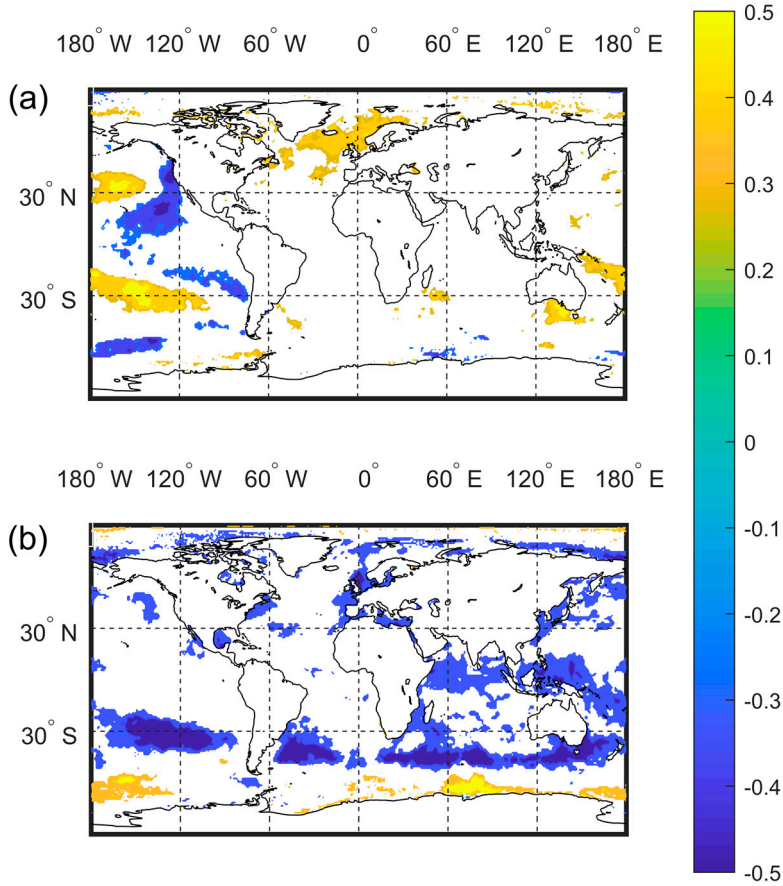


Figure 9. Spearman correlation between PCs of the rainy season precipitation in the SRYR and annual average SST: (a) PC1; (b) PC2.

In view of the above, the results support the hypothesis that rainy season precipitation over the SRYR is strongly influenced by an integrated effect of ENSO and PDO teleconnections. During PDO cold/warm phase (expressed as negative/positive PDO index), the SRYR experiences an increase/decrease of rainy season precipitation. For SOI, the conditions are the opposite: during SOI cold/warm phase (expressed as negative/positive SOI index), the SRYR experiences a decrease/increase of rainy season precipitation.

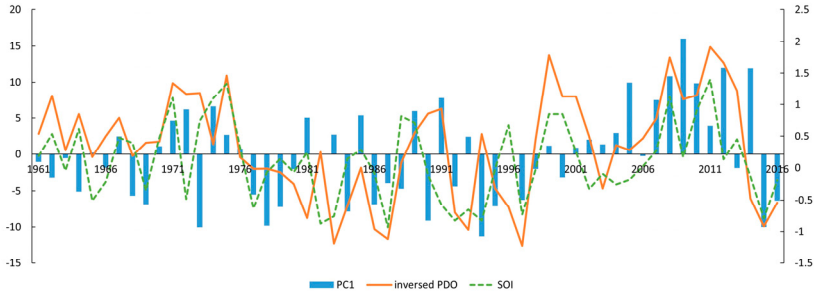


Figure 10. Time series of PC1 with inverted PDO index (solid line) and SOI index (broken line).

6.2.2. Integrated impact of large-scale circulation for rainy season

To evaluate the integrated effects of ENSO and PDO, four periods were identified by considering all possible combinations of PDO and SOI phases (**Paper II**). The PDO phases were identified using a three-month average (June-August; JJA) PDO index series with 11-year moving average to filter the long-term evolution, which is in accordance with Mantua and Hare (2002) and Easterbrook (2016). The SOI phases are identified by average JJA SOI index series, which is consistent with ENSO years (<https://ggweather.com/enso/oni.htm>). Four scenarios were generated based on the combination of PDO/SOI phases (Table 5).

Table 5. Positive (+) and negative (-) phases of PDO and SOI and combinations.

Phase	Period
PDO-	1961-1976, 1999-2016
PDO+	1977-1998
SOI-	1963, 1965, 1966, 1969, 1972, 1977, 1978, 1979, 1980, 1982, 1983, 1986, 1987, 1990-1994, 1997, 2002-2004, 2006, 2009, 2014-2015
SOI+	1961, 1962, 1964, 1967, 1968, 1970, 1971, 1973-1976, 1981, 1984, 1985, 1988, 1989, 1995, 1996, 1998, 1999-2001, 2005, 2007, 2008, 2010-2013, 2016
Combination*	Period
PDO-/SOI-	1963, 1965, 1966, 1969, 1972, 2002-2004, 2006, 2009, 2014, 2015
PDO-/SOI+	1961, 1962, 1964, 1967, 1968, 1970, 1971, 1973-1976, 1999-2001, 2005, 2007, 2008, 2010-2013, 2016
PDO+/SOI-	1977, 1978-1980, 1982, 1983, 1986, 1987, 1990-1994, 1997
PDO+/SOI+	1981, 1984, 1985, 1988, 1989, 1995, 1996, 1998
* PDO-/SOI- and PDO+/SOI+ are referred to as in-phase scenarios, and PDO-/SOI+ and PDO+/SOI- are referred to as out-of-phase scenarios in the text.	

Figure 11 (a-d) shows the composites of rainy season precipitation anomalies for negative PDO with different SOI phases. Negative PDO results in more precipitation for the entire basin with a mean anomaly of +11.0 mm (Figure 11.a). Composites reveal that the precipitation variation induced by negative PDO is altered with respect to the SOI phase. For negative SOI years (Figure 11.b), the precipitation anomaly shows a pattern (mean anomaly +10.2 mm) with even more precipitation in the western part of SRYR but less precipitation in the east compared to that depicted in Figure 11.a. In contrast, negative PDO years occurring with a positive SOI phase (Figure 11.c) show a pattern with an increased mean anomaly of +12.8 mm especially in the eastern part. Comparing with the anomaly between in- and out-of-phase scenarios (Figure 11.d), precipitation under out-of-phase scenario (PDO-/SOI+) tends to be less than precipitation under in-phase scenario (PDO-/SOI-) in western areas of SRYR (mean anomaly -7.7 mm), and the opposite result occurs in the eastern and the far southwestern part (mean anomaly 11.6 mm). To conclude, negative PDO induces more precipitation in SRYR, and the influence is enhanced with a positive SOI phase (La Niña) and compensated with a negative SOI phase (El Niño) in the eastern parts of SRYR, while in the western parts, the opposite case is true.

Figure 11 (e-h) shows the precipitation anomaly in a similar manner as in Figure 11 (a-d), but only for the positive PDO and SOI composite phase. Positive PDO results in less precipitation for the entire basin (maximum reduction in the central parts) with a mean anomaly of -17.0 mm (Figure 11.e). Composites with respect to the SOI phase reveal that precipitation reduction related to positive PDO is accentuated by a positive SOI phase (Figure 11.f). This gives a pattern with weaker anomaly (mean anomaly -4.0 mm) as compared to Figure 11.e: in the central area, negative precipitation anomalies are smaller; in the surrounding area, even opposite anomalies occur. In contrast, precipitation reduction triggered by a positive PDO is reinforced by the negative SOI phase (Figure 11.g). In such years, a similar but stronger precipitation decrease is produced (mean anomaly -24.4 mm) compared to that depicted in Figure 11.e. Comparing the anomaly between in- and out-of-phase scenarios, notable differences are exhibited (Figure 11.h). Precipitation under out-of-phase scenario (PDO+/SOI-) tends to be much less than precipitation under in-phase scenario (PDO+/SOI+) for almost the entire basin (mean anomaly -21.2 mm). Above all, positive SOI phase triggers more precipitation (La Niña), which impairs the influence of positive PDO, and negative SOI phase (El Niño) enhances the precipitation reduction induced by a positive PDO.

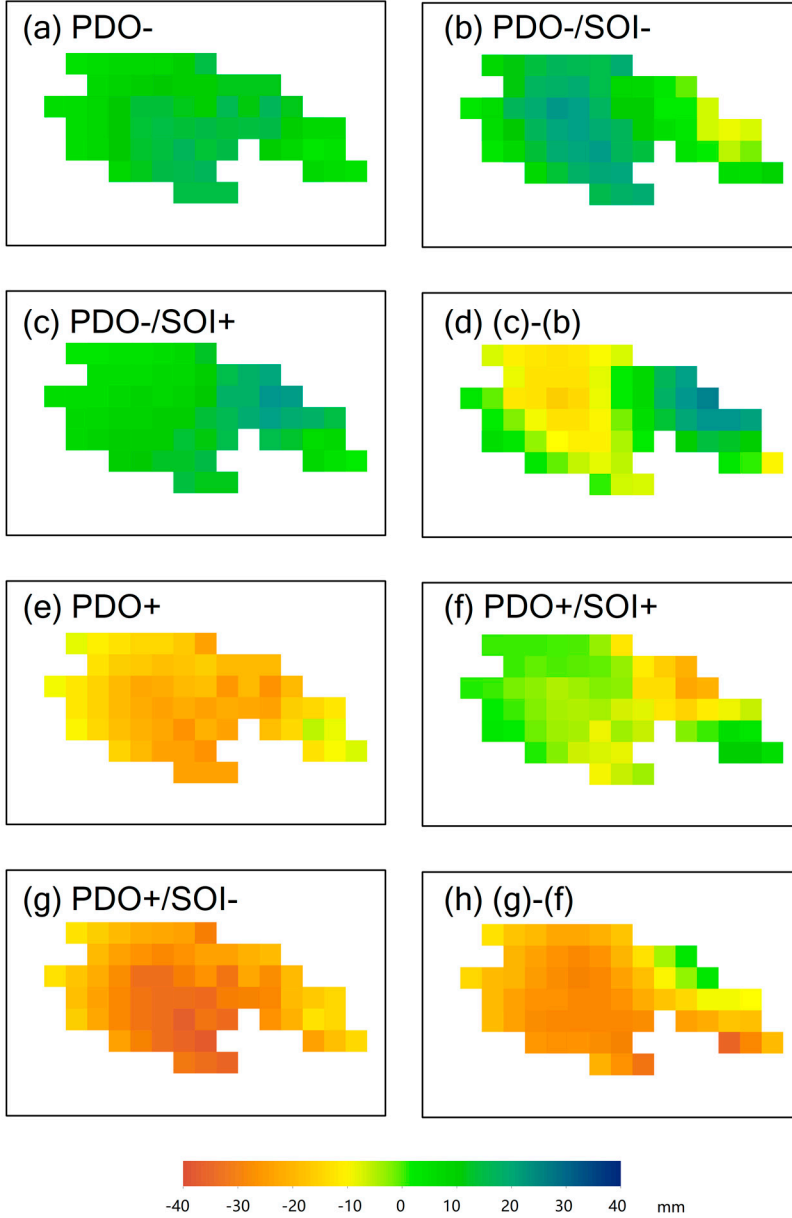


Figure 11. Precipitation anomalies under different scenarios: (a) PDO-; (b) PDO-/SOI-; (c) PDO-/SOI+; (d) difference between out-of-phase and in-phase, i.e., (c)-(b); (e) PDO+, (f) PDO+/SOI+, (g) PDO+/SOI-, and (h) difference between out-of-phase and in-phase, i.e., (g)-(f).

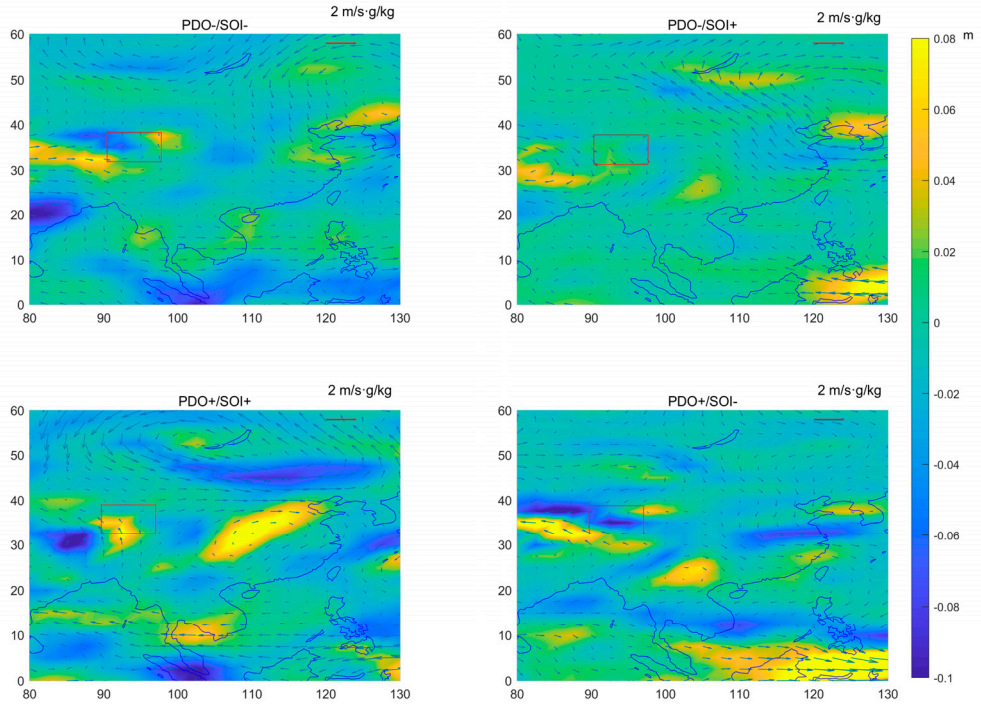


Figure 12. Composites of moisture flux (blue arrow) at 500 mb with MFC (color shading) under different scenarios: red rectangle represents the domain of the SRYR; red arrow represents reference vector of 2 m/s·g/kg.

A possible physical mechanism for the integrated influence can be summarized through occurrence of the moisture flux at 500 mb together with horizontal moisture flux convergence (MFC) under different scenarios (Figure 12). During PDO-/SOI- and PDO-/SOI+, a strong moisture flux transport from west into the study area can be observed (Figure 12, upper). This can be interpreted as a strengthening of the westerlies. This finds support from previous research. An intensified wave train via western central Asia propagates during negative PDO. Together with an enhanced and northward-shifted Western Pacific Subtropical High, this brings more precipitation to northern China (Zhang et al., 2018). The MFC patterns show both positive and negative values in the SRYR domain during PDO-/SOI- and PDO-/SOI+ scenarios. This tends to lead to both convergence and divergence events in the SRYR, which explains the spatial variation of precipitation in the study area. During PDO+/SOI+ years (Figure 12, lower-left), a southern anomaly of moisture flux can be observed across the SRYR domain, which is likely to be blocked by the Himalayan mountains. Even with positive MFC, precipitation does not tend to form in the SRYR. As for PDO+/SOI- years (Figure 12, lower-right), moisture flux from the south divides as it reaches the SRYR. One part is moving eastwards to the Indian

subcontinent while the other moves westwards to southwestern China. Therefore, a subsidence zone is formed in the SRYR domain with a negative MFC, which does not promote formation of precipitation and therefore gives less precipitation in this area. These results confirm the interpretation of Fu et al. (2008) that precipitation decreases in northern China during a warm PDO phase. This situation leads to water vapor transport from Bay of Bengal to southern China and less to northern China. As well, Qian and Zhou (2014) showed that under a PDO+ phase, north China is dominated by an anomalous high pressure and thus deficient precipitation is seen here.

6.2.3. Simulation of precipitation using large-scale circulation

Simulation of precipitation using significantly correlated large-scale circulation indices was established in **Paper III**. Before setting up the simulation models, PCA analysis was conducted for the precipitation datasets of each season separately. PCs were used as simulating targets instead of the original data. In this way, the number of targets was reduced from 64 grids to 3 PCs, and over-fitting was avoided since noise is filtered out. The similarity between each model was minimized since PCs are uncorrelated. Thus, time series of 64 grids over the basin for seasonal precipitation anomalies were subjected to PCA. The leading three PCs for different seasons explain about 91, 92, 90, and 87% (Table 6) of the total variance, respectively. These were retained for further analysis.

Table 6. Explained variance of leading PCs for seasonal precipitation.

%	PC1	PC2	PC3	Cumulative
MAM	71.4	11.2	8.1	90.7
JJA	64.3	19.6	8.5	92.4
SON	65.6	15.4	9.2	90.2
DJF	63.1	14.0	10.0	87.1

Spearman rank correlation (ρ) was calculated to reveal the association between climate indices and PCs of each season. To consider nonlinear relationships between regional climate indices and local precipitation, correlation analyses were conducted for both concurrent and lagged time periods (lag_0= current quarter, lag_i= i quarter(s) ahead). Changing climate indices were assumed to give changes for present or future precipitation patterns.

Based on Spearman rank correlation results, the most significantly influencing lag of each significant climate index was selected as potential predictor ($p < 0.05$). The results for these potential predictors are shown in Table 7. Since PC1 for each season represents the largest precipitation variance, potential predictors for PC1 are essential for the success of prediction. For spring (MAM), SOI_1, NAO_3, and

POL_4 were the significant indices for PC1. For summer PC1 (JJA), NAO_0, PDO_1, SOI_3 were the most significant indices. The only potential predictor for autumn (SON) PC1 was POL_1. For winter (DJF), SCA_0, NAO_0, PDO_3 can be used to predict PC1. Similarly, predictors for PC2 and PC3 can be selected, while Spring PC2 and winter PC3 have no available predictor among the studied climate indices. All potential predictors were used as initial inputs for simulation in ANN and MLR models. For the MLR model, a stepwise method performed further selection among the potential predictors.

The performance of ANN and MLR was compared by three-fold cross-validation. The average performance (MAE, RMSE, and COR) of three tests avoids uncertainty caused by sample selection. From the view of MAE and RMSE, each model has its advantages in different seasons. The average performance for all predicted variables gives ANN an edge over MLR as both MAE and RMSE for ANN were smaller (0.319 to 0.325, and 0.416 to 0.417, respectively). From the view of COR (correlation coefficient), ANN was clearly superior to MLR as COR for each predicted variable was higher for ANN (0.455 to 0.301). As a result, ANN was selected to be the better predictive model for precipitation in the SRYR.

The ANN model was trained using the entire dataset, and the structure for the optimal model was: Levenberg-Marquardt as the training algorithm; 2 to 4 as the neuron number (Table 7); tansig as the activation function for the hidden layer; and linear activation function for the output layer. The performance of the ANN models is shown in Table 7. Based on COR between target and simulated records, all predictands simulated by ANN showed good performance with significant COR ($p < 0.05$) for all PCs. For PC1 in each season, results of COR were between 0.729 and 0.995, indicating high prediction capacity.

Table 7. Performance and structure of the predictive ANN model.

	Predictand	Predictor	ANN Prediction			
			Structure (input/hidden/output)	MAE	RMSE	COR
MAM	PC1	SOI_1,NAO_3,POL_4	3/4/1	0.062	0.106	0.969
	PC3	SCA_0,PNA_1,SOI_2,PDO_2	4/4/1	0.024	0.044	0.993
JJA	PC1	NAO_0,PDO_1,SOI_3	3/4/1	0.070	0.127	0.962
	PC2	SCA_1,PNA_4	2/3/1	0.018	0.033	0.996
	PC3	POL_0	1/2/1	0.183	0.288	0.764
SON	PC1	POL_1	1/2/1	0.201	0.300	0.729
	PC2	SOI_2,PDO_2	2/3/1	0.043	0.085	0.977
	PC3	SOI_4,POL_4	2/3/1	0.110	0.168	0.918
DJF	PC1	SCA_0,NAO_0,PDO_3	3/4/1	0.037	0.051	0.995
	PC2	POL_1	1/2/1	0.146	0.246	0.652

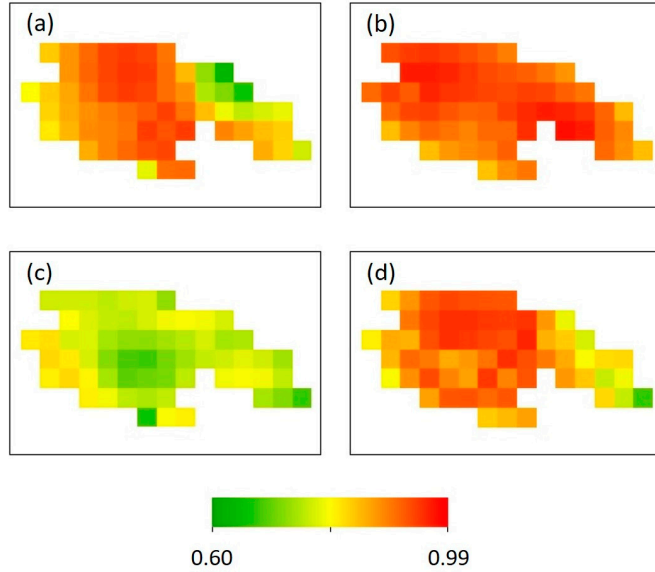


Figure 13. Pearson correlation between original and PCA-ANN simulated precipitation anomalies; (a) spring, (b) summer, (c) autumn, and (d) winter.

To validate the performance of the models with regard to spatial distribution, simulated precipitation was derived by reconstruction using simulated PCs. Pearson correlation coefficients between the original and simulated datasets are shown in Figure 13. Correlation coefficients for all seasons (Figure 13a-13d) showed significant results over the whole basin ($p < 0.05$), with the mean coefficient as 0.872 for spring, 0.922 for summer, 0.762 for autumn, and 0.881 for winter. This shows the overall capability of capturing the spatial distribution of precipitation using PCA-ANN models. With these results, the ranking of PCA-ANN model performance is summer > winter > spring > autumn. The results in summer provide powerful support that the PCA-ANN model is capable of application in SRYR as summer is the rainy season with over 70% of the annual precipitation. In winter and spring, as less precipitation occurs during this season, the precipitation pattern is less complicated compared to other seasons, by which the model is able to capture the variability efficiently. In autumn, the models show less good performance, and the reason could be the complex conditions of atmospheric circulation during this season. Autumn is characterized by a transformation of the atmospheric circulation between southeasterly winds (summer) to northwesterly winds (winter). In any case, we conclude that the PCA-ANN model is capable of predicting precipitation in the SRYR with good results. The ability to predict seasonal precipitation using climate indices makes the PCA-ANN model a significant tool that can contribute to water resources management in this area.

6.3. Future precipitation pattern

6.3.1. Performance evaluation

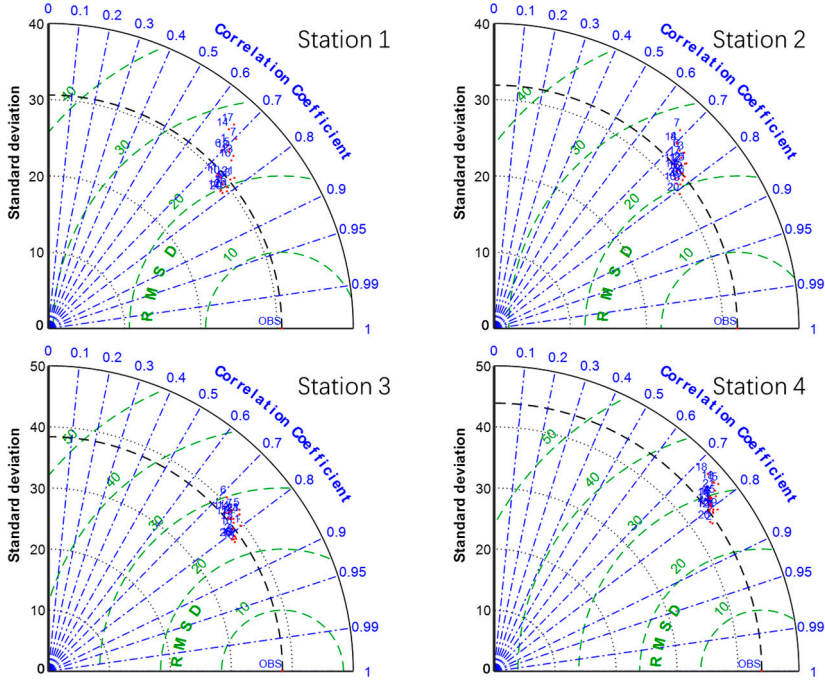


Figure 14. Taylor diagram of 21 individual NEX-GDDP models. OBS denotes the statistics of observed data, 1 to 21 denotes the 21 models listed in Table 3.

Performance of NEX-GDDP dataset was evaluated and presented in **Paper IV**. Figure 14 shows the Taylor diagram which presents three statistics (the COR, RMSD, and SD) of individual models and observations. The figure shows the 21 NEX-GDDP models used in our study compared with the observations on a monthly scale. Generally, the closer to the observation (OBS) point, the better the performance. For Station 1 (Wudaoliang), the models perform overall well as the CORs range from 0.672 to 0.793, the RMSDs range from 19.4 to 27.5 mm, and the differences to observed SD range from -1.73 to 5.55 mm. For station 2 (Tuotuohe), all 21 models show a CORs between 0.684 and 0.810, RMSDs between 19.2 and 27.1 mm, and differences to observed SD between -1.83 and 3.74 mm. For station 3 (Qumalai), the models also show good performance as CORs reach 0.716- 0.822, RMSDs range 22.5-30.0 mm, and the differences to observed SD reach -1.38-2.67 mm. For station 4 (Yushu), the models overall perform well as CORs reach 0.731 to 0.827, RMSDs range from 25.4 to 33.4 mm, and the differences to observed SD range between -1.58 and 3.30 mm.

Station 1					Station 2					Rank
Model No.	COR	RMSD	ΔSD	RI	Model No.	COR	RMSD	ΔSD	RI	
19	0.793	19.38	1.085	0.825	9	0.791	19.18	0.036	0.921	1
15	0.784	19.88	0.739	0.794	20	0.810	22.65	0.724	0.667	2
20	0.789	19.40	1.670	0.762	8	0.777	21.06	1.153	0.635	3
8	0.774	20.68	0.220	0.746	16	0.783	23.56	0.057	0.619	4
9	0.768	20.67	0.532	0.714	2	0.771	22.15	0.239	0.603	5
2	0.780	19.81	1.619	0.698	5	0.757	20.33	1.108	0.587	6
12	0.781	19.75	1.728	0.698	13	0.773	21.76	1.040	0.587	7
3	0.771	20.41	0.991	0.651	15	0.767	21.56	0.762	0.587	8
21	0.777	20.71	0.776	0.651	19	0.786	20.75	2.243	0.571	9
10	0.752	21.39	0.559	0.603	21	0.759	22.95	0.031	0.571	10
4	0.765	20.70	0.918	0.587	1	0.761	22.71	0.227	0.540	11
11	0.740	21.86	0.602	0.556	10	0.783	25.50	0.446	0.524	12
16	0.737	23.01	1.971	0.381	14	0.757	20.61	2.058	0.476	13
13	0.731	23.51	2.578	0.302	3	0.735	22.67	0.113	0.460	14
18	0.715	24.20	2.514	0.286	12	0.753	21.08	1.795	0.429	15
5	0.711	24.54	2.899	0.222	7	0.684	22.07	1.368	0.270	16
6	0.696	24.70	1.989	0.206	4	0.702	21.24	3.737	0.238	17
1	0.698	25.08	2.922	0.143	18	0.704	24.08	1.319	0.222	18
7	0.704	25.56	4.371	0.127	11	0.744	27.06	1.328	0.206	19
14	0.672	27.03	4.640	0.032	17	0.739	24.53	2.204	0.159	20
17	0.673	27.47	5.548	0.016	6	0.722	25.60	1.831	0.127	21
Station 3					Station 4					
Model No.	COR	RMSD	ΔSD	RI	Model No.	COR	RMSD	ΔSD	RI	
12	0.817	22.99	0.730	0.810	9	0.809	27.03	0.322	0.810	
3	0.812	23.35	0.673	0.746	7	0.806	27.25	0.222	0.794	
10	0.822	22.56	1.224	0.730	1	0.803	27.57	0.043	0.762	
16	0.791	24.80	0.107	0.714	2	0.827	25.45	1.404	0.746	
19	0.815	23.04	1.102	0.698	19	0.809	27.35	0.604	0.714	
9	0.809	23.51	0.737	0.667	14	0.795	28.09	0.025	0.698	
13	0.781	25.59	0.515	0.635	20	0.822	25.78	1.584	0.698	
20	0.813	23.09	1.384	0.619	10	0.799	27.71	0.456	0.635	
2	0.800	24.00	1.020	0.603	12	0.801	27.52	0.639	0.635	
1	0.798	24.80	1.093	0.540	13	0.790	28.51	0.102	0.619	
4	0.769	26.28	0.594	0.508	3	0.790	28.52	0.290	0.587	
17	0.762	26.60	0.316	0.476	16	0.781	29.21	0.502	0.460	
15	0.773	26.20	0.908	0.460	17	0.782	29.29	0.927	0.397	
8	0.765	26.55	0.678	0.444	6	0.779	29.50	0.910	0.365	
11	0.746	27.56	0.521	0.317	15	0.782	29.55	1.699	0.317	
18	0.774	26.61	2.096	0.302	4	0.775	29.74	0.929	0.286	
21	0.774	26.62	2.112	0.254	21	0.771	30.48	2.153	0.190	
14	0.752	27.47	1.168	0.190	8	0.756	31.75	2.881	0.111	
5	0.764	27.36	2.611	0.143	5	0.765	31.41	3.300	0.095	
7	0.752	27.65	1.678	0.127	11	0.754	31.91	2.916	0.063	
6	0.716	29.91	2.432	0.016	18	0.731	33.42	3.090	0.016	

Figure 15. Rankings of 21 individual NEX-GDDP models for four stations with COR, RMSD (mm), ΔSD (mm), and RI. |ΔSD| denotes the absolute value of ΔSD.

Figure 15 shows the ranking of the 21 NEX-GDDP models at each station. Green denotes higher ranking, and yellow denotes lower ranking. Comprehensive index RI is calculated for each model. For station 1 (Wudaoliang), the top five ranked models are No. 19, 15, 20, 8, and 9. For station 2 (Tuotuohe) they are No. 9, 20, 8, 16, and 2. For station 3 (Qumalai) they are No. 12, 3, 10, 16, and 19. For station 4 (Yushu) they are No. 9, 7, 1, 2, and 19. In this way, COR, RMSD, and SD are considered. Names of top performing models are shown in Table 8.

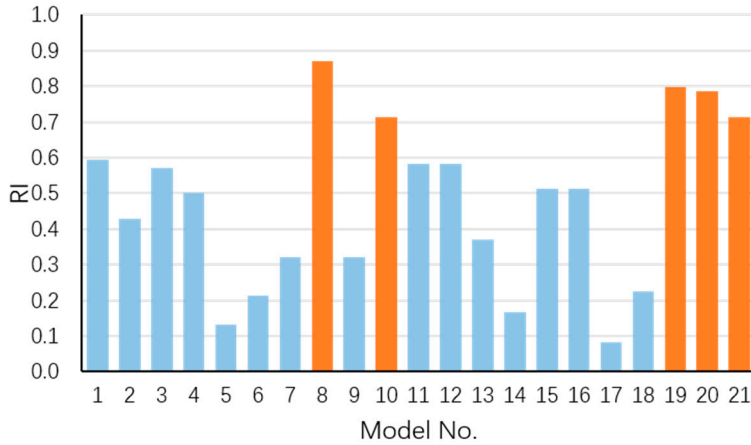


Figure 16. Comprehensive ranking index (RI) of 21 individual NEX-GDDP models for the basin. Orange denotes the top 5 models.

For the basin model, a comprehensive ranking index (RI) considering rankings at each station is conducted (Figure 16). The top 5 models are No. 8, 19, 20, 21, and 10. Names of these models are shown in Table 8. The results provide references for the using of NEX-GDDP dataset in this area.

Table 8. The top five models with best performance for each station and the SRYR.

	Station 1	Station 2	Station 3	Station 4	Basin
1	NorESM1-M	GFDL-ESM2G	IPSL-CM5A-MR	GFDL-ESM2G	GFDL-CM3
2	MIROC5	bcc-csm1-1	CCSM4	CanESM2	NorESM1-M
3	bcc-csm1-1	GFDL-CM3	GFDL-ESM2M	ACCESS1-0	bcc-csm1-1
4	GFDL-CM3	MPI-ESM-LR	MPI-ESM-LR	BNU-ESM	inmcm4
5	GFDL-ESM2G	BNU-ESM	NorESM1-M	NorESM1-M	GFDL-ESM2M

6.3.2. Projections of the future

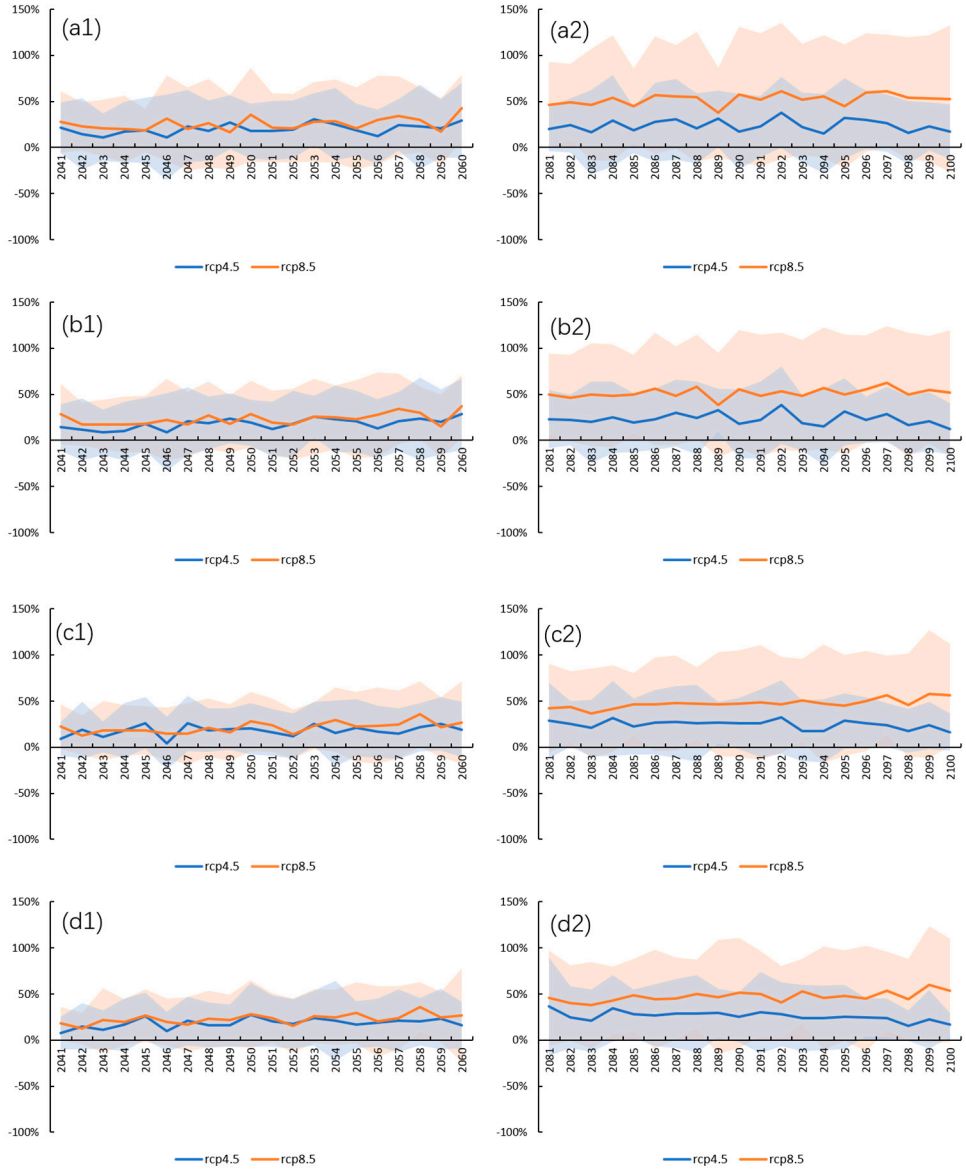


Figure 17. Annual precipitation change in near- and far-future periods under RCP 4.5 (blue) and RCP 8.5 (red) scenarios from the multi-model ensemble (MME) mean (solid line) with one inter-model standard deviation (shading): (a) station 1, (b) station 2, (c) station 3, (d) station 4; (1) near-future period, (2) far-future period.

Taking 1986-2005 as the historical baseline, annual precipitation change for future periods at each station in the SRYR was derived based on the multi-model ensemble (MME) of all 21 models and the results are depicted by solid lines in Figure 17. It is seen that the annual precipitation continues to increase in the near- (2041-2060) and far-future (2081-2100) periods under RCP 4.5 and RCP 8.5 scenarios, with the strongest and most continuous increase under RCP 8.5, and flattened increase under RCP 4.5. The difference of precipitation changing ratios between the two scenarios is small in the near-future period and expands in the far-future period. In the near-future period, the annual precipitation increases ~20% under RCP 4.5 and ~30% under RCP 8.5, relative to the reference period. While in the far-future period, the increased annual precipitation rises to ~30% for RCP 4.5 and ~50% for RCP 8.5.

Uncertainty boundaries are shown by one inter-model SD with the MME model-ensemble precipitation (color shading in Figure 17). The results show a remarkable increase in uncertainty at four stations under both emission scenarios, with larger uncertainty under RCP 8.5 and smaller under RCP 4.5. For example, at Station Wudaoliang (Station 1, Figure 17.a1, a2): in the near-future, the average SD under RCP 8.5 ($\pm 39\%$) are 1.1 times that under RCP 4.5 ($\pm 34\%$), while in the far-future the average SD under RCP 8.5 ($\pm 62\%$) are 1.7 times that under RCP 4.5 ($\pm 36\%$).

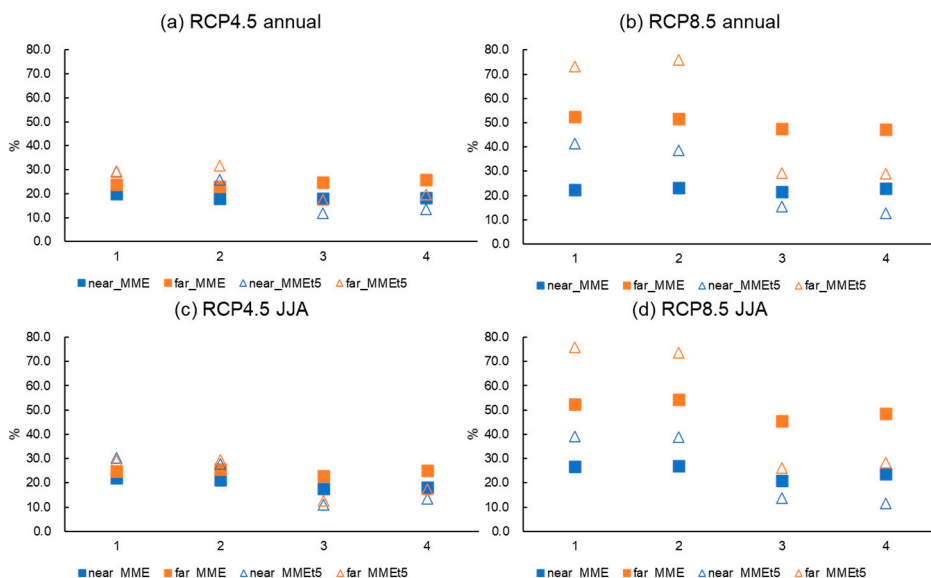


Figure 18. Change ratios (%) for annual precipitation (a,b) and summer precipitation (JJA) (c,d) at each station under two different scenarios. (a)(c) are under RCP 4.5, (b)(d) are under RCP 8.5. Color blue denotes results for the near-future. Color orange denotes results for the far-future. Square denotes results of MME. Triangle denotes results of MMEt5.

To further compare the ensemble results for annual and summer precipitation, change ratios for future precipitation at each station in the SRYR was derived based on the multi-model ensemble of all 21 models (MME) and top-5 models (MMet5), respectively. The results are in Figure 18. Based on MME results (squares in Figure 18.a and b), the increase of annual precipitation at four stations during the near-future (2041-2060) and the far-future (2081-2100) shows an average amplitude of +18.6% and +24.4% under RCP 4.5, and a larger increase under RCP 8.5 of +22.5% and +49.7%. The change percentage of summer precipitation (JJA, squares in Figure 18. c and d) show similar results as the annual precipitation but with a slightly larger amplitude: the average increase under RCP 4.5 is +19.8% and +24.5% during the near- and far-future; the average increase under RCP 8.5 is +24.5% and +50.7% for the near- and far-future.

The results of top-5 model ensembles (MMet5) give different insights. For Station 1 and 2, MMEt5 give higher increase than MME. Under RCP 4.5, MMEt5 give ~8% higher increase than MME during the near-future, and ~7% higher increase during the far-future (Figure 18.a). While under RCP 8.5, this difference expands to ~17% and ~22% for near- and far-future, respectively (Figure 18.b). For Station 3 and 4, however, the MMEt5 give smaller increase than MME. Under RCP 4.5, MMEt5 give ~5% lower increase than MME during the near-future, and ~7% lower increase during the far-future (Figure 18.a). While under RCP 8.5, this difference expands to ~8% and ~18% for near- and far-future, respectively (Figure 18.b). The difference of change ratios in summer precipitation between MMEt5 and MME is similar to the difference in annual precipitation (Figure 18.c and d).

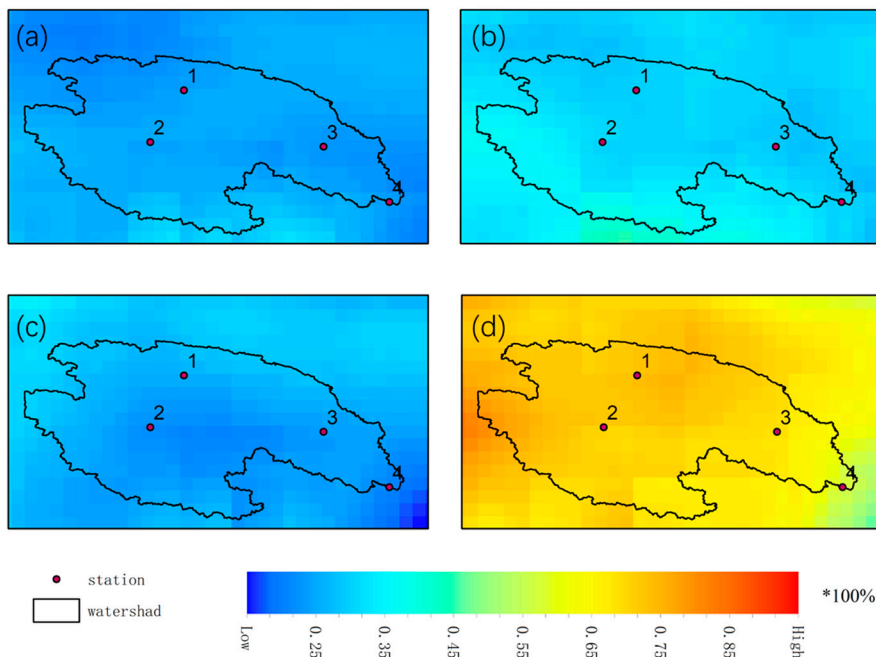


Figure 19. Spatial distribution of annual precipitation change under RCP 4.5 and RCP 8.5 for near- and far-future period from MMEt5 ensemble. (a) 2041-2060 RCP 4.5; (b) 2041-2060 RCP 8.5; (c) 2081-2100 RCP 4.5; (d) 2081-2100 RCP 8.5.

Figure 19 shows the spatial distribution of the annual precipitation changes over the SRYR in the near-future (2041-2060) and far-future (2081-2100) periods, under the RCP 4.5 and RCP 8.5 scenarios, averaged from the top 5 models (MMEt5). Figure 19. a, b and c show a general homogenous increasing pattern across the SRYR with spatial distribution of increasing extent. Figure 19.d shows similar pattern across the SRYR but with larger magnitude in the central basin, which suggests that the most predominant increase in precipitation is expected to occur in the central part of the study area under RCP 8.5 by the end of the 21st century.

Based on the information above, precipitation in the SRYR show a great increase in the future scenarios. The difference between RCP scenarios is smaller in the near-future period, but this difference expands in the far-future period, indicating that the projected change in precipitation is sensitive to the emission scenarios in the far-future. Moreover, the considerable increase results of MMEt5 in Station 1 and 2 necessitate more attention to the central area of the SRYR.

7. Conclusions and outlook

7.1. Conclusions

This study improved the physical understanding of hydroclimatic change in the source region of the Yangtze River (SRYR) from the impacts of large-scale circulation patterns and visualized future projections of precipitation change. The assessment of precipitation variation in the SRYR was conducted in terms of change and variability.

Firstly, the historical change of hydro-climatic components between 1957-2013 was analysed in the SRYR in Paper I. Results show that the annual temperature, precipitation and evapotranspiration increase significantly by 0.34°C, 11.4 mm and 7.6 mm/decade, respectively. The runoff depth increases by 3.3 mm/decade. Considering water balances, annual water storage change was investigated and shows almost constant characteristics despite a continuous small negative trend. The increase of precipitation is mainly offset by the increase of evapotranspiration derived from significantly increasing temperature, leading to the relatively stable water storage during the study period. This knowledge is essential for the understanding of water resources conditions in the study area.

Secondly, analysis of precipitation variability in relation to SST anomalies as well as large-scale circulations including ENSO and PDO was conducted in Paper II. Results indicate that the leading modes of rainy season precipitation variability can be explained by the variability of SST together with an integrated effect of ENSO and PDO. Results show that the influence of ENSO and PDO will increase/decrease when they are in-/out-of-phase. Negative PDO induces more precipitation in La Niña years than in El Niño years for the SRYR, especially over central and eastern parts of the basin. Positive PDO induces precipitation decrease, and El Niño enhances the decrease. The mechanism behind this pattern is atmospheric circulation affecting the strength of westerlies that transports moisture to the inland areas and as well local convergence conditions. Our results have implications for predicting the rainy season precipitation for coming decades over the SRYR. If the current negative PDO phase continues together with more frequent extreme La Niña events, as suggested in previous research (Lapp et al., 2012, Cai et al., 2015, Lin et al., 2018), more precipitation during rainy season is expected over the SRYR.

To further quantify the precipitation variability, Paper III aimed to develop a multi-space model for seasonal precipitation prediction applied to the SRYR with a minimum loss of information. Firstly, the study concluded that the most important climate indices for precipitation in the SRYR vary depending on the season and spatial location. The NAO, POL, SOI, and SCA events have an influence on precipitation in the SRYR during the cold season, while NAO, PDO, and SOI are more important for the warm season. Another important outcome of this study is the spatiotemporal model for predicting grid precipitation, the PCA-ANN model. Our results show that the PCA-ANN model is capable of predicting precipitation in the SRYR using climate indices for the gridded dataset. By reconstruction of PCs, the model provides a simulated dataset with the same size as the original dataset. According to model evaluation, the PCA-ANN model provides good performance in terms of both temporal variability and spatial distribution following the rank summer > winter > spring > autumn. Based on our results, a small basin with a large number of variables/grids is recommended for the PCA-ANN model. In addition, it should be noted that in our results, not all predictors are lagged climate indices. The concurrent climate indices demand additional variables when predicting precipitation. Although, the potential predictability of these climate indices is uncertain, recent studies show some confidence in short-term forecasting up to 8 months (Collins et al., 2002, Visbeck et al., 2001, Miller et al., 2006, Lapp et al., 2012). Based on these results, we are able to use synchronized climate indices to predict seasonal precipitation anomalies in the SRYR.

Finally, to access the future precipitation pattern, Paper IV investigated future climate projections of precipitation in the SRYR after evaluating historical performance, using the NEX-GDDP dataset that provides statistically downscaled CMIP5 projections. Performance for the historical period 1961–2005 was compared against in situ observations. Future climate change was assessed over the future time slices, 2041–2060 and 2081–2100, under two RCP 4.5 and RCP 8.5 with respect to 1986–2005. The results show that multi-model ensemble derived from NEX-GDDP data effectively produces observed precipitation magnitude in the study area. The future climate projections indicate a consistent rise in mean precipitation, especially in summer. The average annual precipitation during the near-future (2041–2060) and the far-future (2081–2100) shows an increase of 18.6% and 24.4% under RCP 4.5, and a larger increase under RCP 8.5 of 22.5% and 49.7%. The summer precipitation shows similar increase as the annual precipitation but with a slightly larger amplitude.

The findings in this thesis provide insights to improve the understanding of water resources variations under the background of climate change, in order to establish a sustainable management of water resources. The precipitation variability in relation to large-scale circulations can help to improve weather forecasting at a low-cost level. Besides, identification of physical mechanisms of integrated impacts from two main circulation patterns can improve the understanding of the forcing behind

precipitation variability. The future projections provide guidance for future adaptive solutions, including both spatial and temporal change. With such information, water resources management plans can be set up with higher accuracy, lower budget, and localized suitability.

7.2. Suggestions

Based on the progresses and results of this thesis, three detailed suggestions are listed considering the local situation.

➤ Aggregate data sharing platform

As the hydrological boundary, geographical boundary, and administrative boundary on the Tibet-Plateau overlap and differentiate from each other, there are several major data platforms that relate to the source region of the Yangtze River. They are operated by different municipalities or research institutions. It would be beneficial for both municipalities and researchers if the datasets can be aggregated into one, however, the cost of resources would be considerable. One solution could be establishing a visualized data index related to different areas. Clicking the interested area, a list of available datasets would show up, with a link accessing to each dataset. Moreover, research results related to a specific area can be listed with references. This ensemble of information can constitute a bridge connecting research and policy makers and help different functional departments to integrate and cooperate.

➤ Identify climate change indicators

Before preparing for the climate change, identification of indicators should be conducted. The indicators can be a large-scale circulation pattern or a type of vegetation or species. The results of this study provide several possible indicators, for example, the ENSO and PDO. Other research results suggest that wetlands could be an indicator as they are sensitive to environmental change (Wang et al., 2020). The sensitivity and effectiveness of possible indicators should be investigated by continuous monitoring and evaluation.

➤ Mitigation and adaptation

Considering the complex and fragile ecosystem, we suggest taking advantage of nature-based ecological restoration. On the basis of national reservation park, more detailed risk area should be identified, and mitigation actions should be carried out based on levels of vulnerability. On the other hand, climate change also provides potential beneficial opportunities. As the results of this thesis reveal that both temperature and precipitation increase, the growing season of grassland could possibly extend. This provides the municipality new potential solutions of local

development, for example, changing from pasture to agriculture. It should be noted that this work should be done in parallel with systematic evaluation of soil moisture as previous research also pointed out the potential risk of dryness under increasing precipitation (Qiang et al., 2018).

7.3. Future studies

Future studies could focus on two aspects. Firstly, regarding seasonal variation of precipitation, there are factors that should be considered besides the atmospheric circulation patterns, including land surface processes and anthropogenic effects (Sutton and Hodson, 2005, Peng et al., 2013, Yang et al., 2008). Further studies on the nonlinear interactions between atmospheric circulation patterns and anthropogenic activities are, in any case, necessary.

Secondly, regarding future precipitation projections, high-resolution climate models provide the possibility of detailed spatial and temporal aspects. The uncertainty that arises from the inherent limitation of the GCM models is still not solved: as the resolution is too coarse, many important processes occur on small spatial scales that cannot be resolved on the model grid (Kendon et al., 2017). A new kind of experiment at very high resolution (< 5 km) could be used to include convection in the models. At this resolution, deep convective storms can be handled but convective plumes are still not resolved, which is called Convection-permitting regional climate model (CPRCM). Advantages of CPRCM have been most evident through improved representation of sub-daily high-intensity precipitation events (Lind et al., 2020). Further studies of CPRCM will provide new insights on assessing precipitation on a regional scale.

References

- BANACOS, P. C. & SCHULTZ, D. M. 2005. The Use of Moisture Flux Convergence in Forecasting Convective Initiation: Historical and Operational Perspectives. *Weather and Forecasting*, 20, 351-366.
- BAO, Y. & WEN, X. 2017. Projection of China's near- and long-term climate in a new high-resolution daily downscaled dataset NEX-GDDP. *Journal of Meteorological Research*.
- BARNSTON, A. G. & LIVEZEY, R. E. 1987. Classification, Seasonality and Persistence of Low-Frequency Atmospheric Circulation Patterns. *Monthly Weather Review*, 115, 1083-1126.
- BIBI, SADIA, WANG, LEI, XIUPING, ZHOU, JING, CHEN, DELIANG & YAO 2018. Climatic and associated cryospheric, biospheric, and hydrological changes on the Tibetan Plateau: a review. *International Journal of Climatology*, 38, e1-e17.
- BUEH, C. & NAKAMURA, H. 2007. Scandinavian pattern and its climatic impact. *Quarterly Journal of the Royal Meteorological Society*, 133, 2117-2131.
- BURN, D. H. & HAG ELNUR, M. A. 2002. Detection of hydrologic trends and variability. *Journal of Hydrology*, 255, 107-122.
- CAI, W., WANG, G., SANTOSO, A., MCPHADEN, M. J., WU, L., JIN, F.-F., TIMMERMAN, A., COLLINS, M., VECCHI, G., LENGAINNE, M., ENGLAND, M. H., DOMMENGET, D., TAKAHASHI, K. & GUILYARDI, E. 2015. Increased frequency of extreme La Niña events under greenhouse warming. *Nature Climate Change*, 5, 132.
- CANEDO-ROSSO, C., UVO, C. B. & BERNDTSSON, R. 2019. Precipitation variability and its relation to climate anomalies in the Bolivian Altiplano. *International Journal of Climatology*, 39, 2096-2107.
- CAO, Q., HAO, Z., YUAN, F., SU, Z., BERNDTSSON, R., HAO, J. & NYIMA, T. 2017. Impact of ENSO regimes on developing- and decaying-phase precipitation during rainy season in China. *Hydrology and Earth System Sciences*, 21, 5415-5426.
- CHELTON, D. B. & RISIEN, C. M. *Zonal and Meridional Discontinuities and Other Issues with the HadISST1.1 Dataset*.
- CHIEW, F. H. S., PIECHOTA, T. C., DRACUP, J. A. & MCMAHON, T. A. 1998. El Niño/Southern Oscillation and Australian rainfall, streamflow and drought: Links and potential for forecasting. *Journal of Hydrology*, 204, 138-149.
- COLLINS, M., FRAME, D., SINHA, B. & WILSON, C. 2002. How far ahead could we predict El Niño? *Geophysical Research Letters*, 29.

- EASTERBROOK, D. J. 2016. Chapter 21 - Using Patterns of Recurring Climate Cycles to Predict Future Climate Changes. *In: EASTERBROOK, D. J. (ed.) Evidence-Based Climate Science (Second Edition)*. Elsevier.
- EKSTROM, J. A., SUATONI, L., COOLEY, S. R., PENDLETON, L. H., WALDBUSSER, G. G., CINNER, J. E., RITTER, J., LANGDON, C., VAN HOOIDONK, R., GLEDHILL, D., WELLMAN, K., BECK, M. W., BRANDER, L. M., RITTSCHOF, D., DOHERTY, C., EDWARDS, P. E. T. & PORTELA, R. 2015. Vulnerability and adaptation of US shellfisheries to ocean acidification. *Nature Climate Change*, 5, 207-214.
- FAZEL, N., BERNDTSSON, R., UVO, C. B., MADANI, K. & KLØVE, B. 2017. Regionalization of precipitation characteristics in Iran's Lake Urmia basin. *Theoretical and Applied Climatology*, 1-11.
- FU, C., JIANG, Z., GUAN, Z., HE, J. & XU, Z.-F. 2008. Regional Climate Studies of China. *Springer Science & Business Media*, 105-110.
- GOCIC, M. & TRAJKOVIC, S. 2014. Analysis of trends in reference evapotranspiration data in a humid climate. *Hydrological Sciences Journal*, 59, 165-180.
- GONG, D. & WANG, S. 1999. Impacts of ENSO on rainfall of global land and China. *Chinese Science Bulletin*, 44, 852-857.
- HAYKIN, S. 1994. *Neural Networks: A Comprehensive Foundation*, Prentice Hall PTR.
- HORNIK, K., STINCHCOMBE, M. & WHITE, H. 1989. Multilayer feedforward networks are universal approximators. *Neural Networks*, 2, 359-366.
- HUTCHINSON, M. F. 1998. Interpolation of Rainfall Data with Thin Plate Smoothing Splines - Part I: Two Dimensional Smoothing of Data with Short Range Correlation. *Journal of Geographic Information and Decision Analysis*, 2, 139-151.
- IPCC 2013. *Climate Change 2013: The Physical Science Basis. Contribution of Working Group I to the Fifth Assessment Report of the Intergovernmental Panel on Climate Change*, Cambridge, United Kingdom and New York, NY, USA, Cambridge University Press.
- JAIN, S., SALUNKE, P., MISHRA, S. K., SAHANY, S. & CHOUDHARY, N. 2019. Advantage of NEX-GDDP over CMIP5 and CORDEX Data: Indian Summer Monsoon. *Atmospheric Research*, 228, 152-160.
- KALNAY, E., KANAMITSU, M., KISTLER, R., COLLINS, W., DEAVEN, D., GANDIN, L., IREDELL, M., SAHA, S., WHITE, G., WOOLLEN, J., ZHU, Y., CHELLIAH, M., EBISUZAKI, W., HIGGINS, W., JANOWIAK, J., MO, K. C., ROPELEWSKI, C., WANG, J., LEETMAA, A., REYNOLDS, R., JENNE, R. & JOSEPH, D. 1996. The NCEP/NCAR 40-Year Reanalysis Project. *Bulletin of the American Meteorological Society*, 77, 437-472.
- KARLSSON, J. M., LYON, S. W. & DESTOUNI, G. 2012. Thermokarst lake, hydrological flow and water balance indicators of permafrost change in Western Siberia. *Journal of Hydrology*, 464, 459-466.
- KENDALL, M. G. 1975. Rank Correlation Methods. *Charles Griffin, London. 4th Edition*, p.202.
- KENDON, E. J., BAN, N., ROBERTS, N. M., FOWLER, H. J., ROBERTS, M. J., CHAN, S. C., EVANS, J. P., FOSSER, G. & WILKINSON, J. M. 2017. Do Convection-

- Permitting Regional Climate Models Improve Projections of Future Precipitation Change? *Bulletin of the American Meteorological Society*, 98, 79-93.
- KNUTSON, T. R., SIRUTIS, J. J., VECCHI, G. A., GARNER, S., ZHAO, M., KIM, H.-S., BENDER, M., TULEYA, R. E., HELD, I. M. & VILLARINI, G. 2013. Dynamical Downscaling Projections of Twenty-First-Century Atlantic Hurricane Activity: CMIP3 and CMIP5 Model-Based Scenarios. *Journal of Climate*, 26, 6591-6617.
- LAPP, S. L., ST. JACQUES, J.-M., BARROW, E. M. & SAUCHYN, D. J. 2012. GCM projections for the Pacific Decadal Oscillation under greenhouse forcing for the early 21st century. *International Journal of Climatology*, 32, 1423-1442.
- LI, L., SHEN, H. Y., DAI, S., LI, H. M. & XIAO, J. S. 2013. Response of water resources to climate change and its future trend in the source region of the Yangtze River. *Journal of Geographical Sciences*, 23, 208-218.
- LIANG, C., HOU, X. B. & PAN, N. 2011. Spatial and temporal variations of precipitation and runoff in the source region of the Yangtze River(in Chinese). *South-to North Transfers and Water Science & Technology*, 0, 35-39.
- LIN, R., ZHENG, F. & DONG, X. 2018. ENSO Frequency Asymmetry and the Pacific Decadal Oscillation in Observations and 19 CMIP5 Models. *Advances in Atmospheric Sciences*, 35, 495-506.
- LIND, P., BELUŠIĆ, D., CHRISTENSEN, O. B., DOBLER, A., KJELLSTRÖM, E., LANDGREN, O., LINDSTEDT, D., MATTE, D., PEDERSEN, R. A., TOIVONEN, E. & WANG, F. 2020. Benefits and added value of convection-permitting climate modeling over Fenno-Scandinavia. *Climate Dynamics*, 55, 1893-1912.
- MANN, H. B. 1945. Nonparametric Tests Against Trend. *Econometrica*, 13, 245-259.
- MANTUA, N. J. & HARE, S. R. 2002. The Pacific Decadal Oscillation. *Journal of Oceanography*, 58, 35-44.
- MAURER, E. P. & HIDALGO, H. G. 2008. Utility of daily vs. monthly large-scale climate data: an intercomparison of two statistical downscaling methods. *Hydrol. Earth Syst. Sci.*, 12, 551-563.
- MEINSHAUSEN, M., SMITH, S. J., CALVIN, K., DANIEL, J. S., KAINUMA, M. L. T., LAMARQUE, J. F., MATSUMOTO, K., MONTZKA, S. A., RAPER, S. C. B., RIAHI, K., THOMSON, A., VELDEERS, G. J. M. & VAN VUUREN, D. P. P. 2011. The RCP greenhouse gas concentrations and their extensions from 1765 to 2300. *Climatic Change*, 109, 213.
- MILLER, R. L., SCHMIDT, G. A. & SHINDELL, D. T. 2006. Forced annular variations in the 20th century Intergovernmental Panel on Climate Change Fourth Assessment Report models. *Journal of Geophysical Research: Atmospheres*, 111.
- MILLS, C. M. & WALSH, J. E. 2013. Seasonal Variation and Spatial Patterns of the Atmospheric Component of the Pacific Decadal Oscillation. *Journal of Climate*, 26, 1575-1594.
- MURPHY, J. 1999. An Evaluation of Statistical and Dynamical Techniques for Downscaling Local Climate. *Journal of Climate*, 12, 2256-2284.
- MYERS, J. L. & WELL, A. D. 2003. Research Design and Statistical Analysis *Lawrence Erlbaum*, 508.

- NOAA 2020. National Centers for Environmental Information, State of the Climate, Global Climate Report for Annual 2019. *retrieved on December 3, 2020 from <https://www.ncdc.noaa.gov/sotc/global/201913>*.
- OUYANG, R., LIU, W., FU, G., LIU, C., HU, L. & WANG, H. 2014. Linkages between ENSO/PDO signals and precipitation, streamflow in China during the last 100 years. *Hydrology and Earth System Sciences*, 18, 3651-3661.
- PAUL, B. K. & RASHID, H. 2017. Chapter Two - Tropical Cyclones and Storm Surges. In: PAUL, B. K. & RASHID, H. (eds.) *Climatic Hazards in Coastal Bangladesh*. Boston: Butterworth-Heinemann.
- PEARSON, K. 1895. Notes on Regression and Inheritance in the Case of Two Parents. *Proceedings of the Royal Society of London*. 58, 240-242.
- PEEL, M. C., FINLAYSON, B. L. & MCMAHON, T. A. 2007. Updated world map of the Köppen-Geiger climate classification. *Hydrology and Earth System Sciences*, 11, 1633-1644.
- PENG, J., YU, Z. & GAUTAM, M. R. 2013. Pacific and Atlantic Ocean influence on the spatiotemporal variability of heavy precipitation in the western United States. *Global and Planetary Change*, 109, 38-45.
- PING, F., LUO, Z. & JU, J. 2006. Differences between dynamics factors for interannual and decadal variations of rainfall over the Yangtze River valley during flood seasons. *Chinese Science Bulletin*, 51, 994-999.
- POWER, S. B. & KOCIUBA, G. 2011. The impact of global warming on the Southern Oscillation Index. *Climate Dynamics*, 37, 1745-1754.
- QIAN, C. & ZHOU, T. 2014. Multidecadal Variability of North China Aridity and Its Relationship to PDO during 1900–2010. *Journal of Climate*, 27, 1210-1222.
- QIAN, K., WANG, X.-S., LV, J. & WAN, L. 2014. The wavelet correlative analysis of climatic impacts on runoff in the source region of Yangtze River, in China. *International Journal of Climatology*, 34, 2019-2032.
- QIANG, ZHANG, KEKE, FAN, VIJAY, SINGH, CHANGQING, SONG & CHONG-YU 2018. Is Himalayan-Tibetan Plateau "drying"? Historical estimations and future trends of surface soil moisture. *The Science of the Total Environment*.
- RAGHAVAN, S. V., HUR, J. & LIONG, S.-Y. 2018. Evaluations of NASA NEX-GDDP data over Southeast Asia: present and future climates. *Climatic Change*, 148, 503-518.
- RANA, A., UVO, C. B., BENGTSSON, L. & SARTHI, P. P. 2012. Trend analysis for rainfall in Delhi and Mumbai, India. *Climate Dynamics*, 38, 45-56.
- RAYNER, N. A., PARKER, D. E., HORTON, E. B., FOLLAND, C. K., ALEXANDER, L. V., ROWELL, D. P., KENT, E. C. & KAPLAN, A. 2003. Global analyses of sea surface temperature, sea ice, and night marine air temperature since the late nineteenth century. *Journal of Geophysical Research: Atmospheres*, 108.
- ROPELEWSKI, C. F. & JONES, P. D. 1987. An Extension of the Tahiti–Darwin Southern Oscillation Index. *Monthly Weather Review*, 115, 2161-2165.

- SAJI, N. H. & YAMAGATA, T. 2003. Structure of SST and Surface Wind Variability during Indian Ocean Dipole Mode Events: COADS Observations. *Journal of Climate*, 16, 2735-2751.
- SHI, F., ZHAO, S., GUO, Z. & GOOSSE, H. 2017. Multi-proxy reconstructions of precipitation field in China over the past 500 years. *Clim. Past Discuss.*, 2017, 1-32.
- SU, F., DUAN, X., CHEN, D., HAO, Z. & CUO, L. 2013. Evaluation of the Global Climate Models in the CMIP5 over the Tibetan Plateau. *Journal of Climate*, 26, 3187-3208.
- SU, M. & WANG, H. 2007. Relationship and its instability of ENSO — Chinese variations in droughts and wet spells. *Science in China Series D: Earth Sciences*, 50, 145-152.
- SUTTON, R. T. & HODSON, D. L. R. 2005. Ocean science: Atlantic Ocean forcing of North American and European summer climate. *Science*, 309, 115-118.
- SUZUKI-PARKER, A. 2012. Uncertainties and limitations in simulating tropical cyclones. *Springer, Berlin*.
- TAKAHASHI, K. & WANG, C. G. 1979. The projection formula for evapotranspiration from the monthly mean temperature and monthly precipitation (in Chinese). *Meteorological Science and Technology*, 26, 29-32.
- TAYLOR, K. E., STOUFFER, R. J. & MEEHL, G. A. 2012. An Overview of CMIP5 and the Experiment Design. *Bulletin of the American Meteorological Society*, 93, 485-498.
- THRASHER, B., MAURER, E. P., MCKELLAR, C. & DUFFY, P. B. 2012. Technical Note: Bias correcting climate model simulated daily temperature extremes with quantile mapping. *Hydrol. Earth Syst. Sci.*, 16, 3309-3314.
- TIAN, Q., PRANGE, M. & MERKEL, U. 2016. Precipitation and temperature changes in the major Chinese river basins during 1957–2013 and links to sea surface temperature. *Journal of Hydrology*, 536, 208-221.
- TRENBERTH, K. E. & HURRELL, J. W. 1994. Decadal atmosphere-ocean variations in the Pacific. *Climate Dynamics*, 9, 303-319.
- UVO, C. B. 2003. Analysis and regionalization of northern european winter precipitation based on its relationship with the North Atlantic oscillation. *International Journal of Climatology*, 23, 1185-1194.
- VISBECK, M. H., HURRELL, J. W., POLVANI, L. & CULLEN, H. M. 2001. The North Atlantic Oscillation: Past, present, and future. *Proceedings of the National Academy of Sciences*, 98, 12876-12877.
- WANG, B., ZHENG, L., LIU, D. L., JI, F., CLARK, A. & YU, Q. 2018. Using multi-model ensembles of CMIP5 global climate models to reproduce observed monthly rainfall and temperature with machine learning methods in Australia. *International Journal of Climatology*, 38, 4891-4902.
- WANG, R., HE, M. & NIU, Z. 2020. Responses of Alpine Wetlands to Climate Changes on the Qinghai-Tibetan Plateau Based on Remote Sensing. *中国地理科学*, 30, 189-201.

- WANG, Y. & XU, X. 2018. Impact of ENSO on the Thermal Condition over the Tibetan Plateau. *Journal of the Meteorological Society of Japan. Ser. II*, advpub.
- WANG, Z., ZENG, Z., LAI, C., LIN, W., WU, X. & CHEN, X. 2017. A regional frequency analysis of precipitation extremes in Mainland China with fuzzy c-means and L-moments approaches. *International Journal of Climatology*, n/a-n/a.
- WASHINGTON, R., HODSON, A., ISAKSSON, E. & MACDONALD, O. 2000. Northern Hemisphere teleconnection indices and the mass balance of Svalbard glaciers. *International Journal of Climatology*, 20, 473-487.
- WEIGEL, A. P., LINIGER, M. A. & APPENZELLER, C. 2008. Can multi-model combination really enhance the prediction skill of probabilistic ensemble forecasts? *Quarterly Journal of the Royal Meteorological Society*, 134, 241-260.
- WOOD, A. W., LEUNG, L. R., SRIDHAR, V. & LETTENMAIER, D. P. 2004. Hydrologic Implications of Dynamical and Statistical Approaches to Downscaling Climate Model Outputs. *Climatic Change*, 62, 189-216.
- XIAO, M., ZHANG, Q. & SINGH, V. P. 2015. Influences of ENSO, NAO, IOD and PDO on seasonal precipitation regimes in the Yangtze River basin, China. *International Journal of Climatology*, 35, 3556-3567.
- XIE, C. W., DING, Y. J., LIU, S. Y. & WANG, G. X. 2003. Comparison Analysis of Runoff Change in the Source Regions of the Yangtze and Yellow Rivers(in Chinese). *Journal of Glaciology and Geocryology*, 25, 414-422.
- YANG, T., ZHANG, Q., CHEN, Y. D., TAO, X., XU, C.-Y. & CHEN, X. 2008. A spatial assessment of hydrologic alteration caused by dam construction in the middle and lower Yellow River, China. *Hydrological Processes*, 22, 3829-3843.
- YAO, T., LIU, X. & WANG, N. 2000. Amplitude of climatic change in Qinghai-Tibetan Plateau. *Chinese ence Bulletin*, 45, 98-106.
- YAO, T., MASSON-DELMOTTE, V., GAO, J., YU, W., YANG, X., RISI, C., STURM, C., WERNER, M., ZHAO, H., HE, Y., REN, W., TIAN, L., SHI, C. & HOU, S. 2013. A review of climatic controls on $\delta^{18}\text{O}$ in precipitation over the Tibetan Plateau: Observations and simulations. *Reviews of Geophysics*, 51, 525-548.
- YAO, Z. J., LIU, Z. F., HUANG, H. Q., LIU, G. H. & WU, S. S. 2014. Statistical estimation of the impacts of glaciers and climate change on river runoff in the headwaters of the Yangtze River. *Quaternary International*, 336, 89-97.
- YUAN, F. 2015. Impacts of climate change on surface hydrology in the source region of the Yellow River. *Doctor, Division of Water Resources Engineering*.
- YUAN, F., BERNDTSSON, R., UVO, C. B., ZHANG, L. & JIANG, P. 2015. Summer precipitation prediction in the source region of the Yellow River using climate indices. *Hydrology Research*, 47, 847-856.
- ZHANG, C., TANG, Q. & CHEN, D. 2016. Recent Changes in the Moisture Source of Precipitation over the Tibetan Plateau. *Journal of Climate*, JCLI-D-15-0842.1.
- ZHANG, G. S., SHI, X. H., LI, D. L., WANG, Q. C. & DAI, S. 2006. Climate change in Tuotuohe Area at the headwaters of Yangtze River(in Chinese). *Journal of Glaciology and Geocryology*, 678-685.

- ZHANG, Y., LIU, S. Y., XU, J. L. & SHANGGUAN, D. H. 2008. Glacier change and glacier runoff variation in the Tuotuo River basin, the source region of Yangtze River in western China. *Environmental Geology*, 56, 59-68.
- ZHANG, Y., WALLACE, J. M. & BATTISTI, D. S. 1997. ENSO-like Interdecadal Variability: 1900–93. *Journal of Climate*, 10, 1004-1020.
- ZHANG, Z., SUN, X. & YANG, X.-Q. 2018. Understanding the Interdecadal Variability of East Asian Summer Monsoon Precipitation: Joint Influence of Three Oceanic Signals. *Journal of Climate*, 31, 5485-5506.